ARMY RESEARCH LABORATORY

A Shear Banding Model for Penetration Calculations

by Martin N. Raftenberg

ARL-TR-2221 April 2000

Army Research Laboratory
Aberdeen Proving Ground, MD 21005-5069

ARL-TR-2221 **April 2000**

A Shear Banding Model for Penetration Calculations

Martin N. Raftenberg
Weapons and Materials Research Directorate, ARL

Abstract

A model for introducing the effects of adiabatic shear banding into a penetration calculation was installed into the EPIC wavecode. These effects are deemed to be reduction in the ratio of flow stress to the value predicted by the Johnson-Cook strength model and increase in spall pressure. A strain-rate- and temperature-dependent instability strain is determined from small-amplitude perturbation of constant-strain-rate simple shear. Imposed alterations in flow stress ratio and spall pressure commence at the "localization strain," separated from the instability strain by a fixed strain increment. The alterations proceed linearly with increasing effective plastic strain and terminate after an additional fixed strain increment, at the "failure strain." The values imposed on the flow stress ratio and the spall pressure at the failure strain are functions of local pressure at the time step when localization strain was reached. The nonzero value imposed on the flow stress ratio in the case of positive localization pressure reflects the phenomenon of fracture suppression within a fully formed shear band. The two fixed strain increments are evaluated from a torsional Kolsky bar test. The pre-shear-banded spall pressure is evaluated from plate-on-plate impact data. The flow stress ratio and spall pressure at and beyond the failure strain introduce two currently "free" parameters. The model was applied to a set of problems involving steel plate perforation by a tungsten rod, and reasonable agreement with experiment was obtainable in terms of the final target hole size and the length and speed of the tungsten residual.

Table of Contents

		Page
	List of Figures	v
	List of Tables	vii
1.	Introduction	1
2.	The Model	2
2.1	Overview	2
2.2	Instability Strain	2
2.3	Localization Strain and Failure Strain	4
2.4	Pressure-Dependent Residual Strength	5
2.5	Spall Strength Reduction	5
3.	An Application	7
3.1	Description of Problems	7
3.2	Description of the Computations	7
3.3	Computational and Experimental Results Compared	10
4.	Concluding Remarks	13
4.1	Summary of Results	13
4.2	Suggestions for Future Work	14
5.	References	39
	List of Symbols	43
	Distribution List	47
	Report Documentation Page	55

INTENTIONALLY LEFT BLANK.

List of Figures

1 The Shear Banding Model. 15
2 An Adiabatic Stress-Strain Curve at Constant Strain Rate. 16
3 Torsional Stress-Strain Curve for HY-100 Steel at Room Temperature and a Constant Strain Rate of 1600 s^{-1}. 17
4 Ductile Voids Within a Shear Band in a U-2Mo Penetrator. 18
5 Sectioned Target Plate from Test 1071. 19
6 Initial Mesh for Problem 1, Superimposed on Digitized Experimental Perforation-Hole Contour With Cavities and Cracks Indicated. 20
7 Final Through-Thickness-Averaged Hole Diameter vs. Spall Pressure of Shear-Banded RHA From Problem 1. 21
8 Final Through-Thickness-Averaged Hole Diameter vs. Spall Pressure of Shear-Banded RHA From Problem 2. 22
9 Final Through-Thickness-Averaged Hole Diameter vs. Spall Pressure of Shear-Banded RHA From Problem 3. 23
10 Final Through-Thickness-Averaged Hole Diameter vs. Spall Pressure of Shear-Banded RHA From Problem 4. 24
11 Final Through-Thickness-Averaged Hole Diameter vs. Spall Pressure of Shear-Banded RHA From Problem 5. 25
12 Final Through-Thickness-Averaged Hole Diameter vs. Spall Pressure of Shear-Banded RHA From Problem 6. 26
13 Final Through-Thickness-Averaged Hole Diameter vs. Striking Speed From Problems 1 Through 6 for $P_{fail}^{(sb)} = -3.0$ GPa and $b_o = 1.0$. 27
14 Residual Rod Length vs. Spall Pressure of Shear-Banded RHA From Problem 2. 28
15 Residual Rod Speed vs. Spall Pressure of Shear-Banded RHA From Problem 2. 29
16 Mesh Plot at 25 μs After Impact From Problem 1 with $P_{fail}^{(sb)} = -3.0$ GPa and $b_o = 0.5$. 30
17 Mesh Plot at 50 μs After Impact From Problem 1 with $P_{fail}^{(sb)} = -3.0$ GPa and $b_o = 0.5$. 31
18 Mesh Plot at 75 μs After Impact From Problem 1 with $P_{fail}^{(sb)} = -3.0$ GPa and $b_o = 0.5$. 32
19 Mesh Plot at 100 μs After Impact From Problem 1 with $P_{fail}^{(sb)} = -3.0$ GPa and $b_o = 0.5$. 33
20 Mesh Plot at 2500 μs After Impact From Problem 1 with $P_{fail}^{(sb)} = -3.0$ GPa and $b_o = 0.5$. 34
21 Final Through-Thickness-Averaged Hole Diameter vs. Striking Speed From Problems 1 Through 6 for $P_{fail}^{(sb)} = -0.2$ GPa and $b_o = 0.5$. 35
22 Residual Rod Length vs. Striking Speed From Problems 1 Through 6 for $P_{fail}^{(sb)} = -0.2$ GPa and $b_o = 0.5$. 36
23 Residual Rod Speed vs. Striking Speed From Problems 1 Through 6 for $P_{fail}^{(sb)} = -0.2$ GPa and $b_o = 0.5$. 37

INTENTIONALLY LEFT BLANK.

List of Tables

1 Estimates of $P_{fail}^{(o)}$ for RHA Corresponding to Reasonable Values of Y 6
2 Six Problems Defined 7
3 Ten Experiments Identified 8
4 Material-Constant Values 9
5 Comparison of Computational and Experimental L_{res} Results 11
6 Comparison of Computational and Experimental v_{res} Results 12
7 Code for Damage Legend on Mesh Plots 13

INTENTIONALLY LEFT BLANK.

1 Introduction

Rolled homogeneous armor (RHA) is a medium-carbon, martensitic, high-strength steel. U.S. Department of Defense (1991) specifies its allowable range of chemical composition, places broad restrictions on the heat treatment regimen, and specifies performance requirements in terms of such metrics as Charpy impact energy and ballistic limit. The maximum weight percent of carbon can be 0.30 for plates up to 50.8-mm thickness, 0.33 for plates between 50.8- and 101.6-mm thickness, and 0.35 for plates of thickness greater than 101.6 mm. For any thickness, the maximum range in weight-percent carbon is 0.10. Some of the other elements present (e.g., Mn, Ni, Cr, Mo) are used to promote formation of martensite (Honeycombe 1981).

In recent U.S. Army Research Laboratory (ARL)experiments involving perforation of RHA plates by copper shaped charge jets, cracks in the remaining RHA target were lined by shear bands, and recovered RHA fragments were bounded by shear bands (Raftenberg and Krause 1999). Shear banding is an important fragmentation mechanism in RHA penetration, yet is generally not represented in the modeling. The result is a tendency to underpredict target hole size (Raftenberg 1996a).

In an axisymmetric penetration calculation with a Lagrangian finite-element wavecode, a 1-mm edge length is a rough lower limit to practical element size. Within a three-node triangular element, the velocity field is given by bilinear shape functions,

$$\left.\begin{aligned} v_r(r,z) &= a_r + b_r\, r + c_r\, z \\ v_z(r,z) &= a_z + b_z\, r + c_z\, z \end{aligned}\right\} , \tag{1}$$

where a_r, b_r, $\cdots$, c_z are constants; v_r and v_z are the radial and axial components, respectively, of velocity; and r and z are the radial and axial coordinates, respectively. The shear bands observed in Raftenberg and Krause (1999) had a thickness of roughly 6 μm, and these shape functions suppress such fine-scaled shear localization. The goal of the shear banding model is to introduce into a 1-mm element effects of shear localization, which are deemed to be reductions in flow stress and spall strength.

If shear bands could be spatially resolved with a sufficiently fine mesh, perhaps a shear banding model would not be needed as an additional ingredient. A flow law with thermal softening would cause local flow stress reduction, and a void growth model with thermal dependence would cause local spall strength reduction. The former effect, flow stress reduction within a spatially resolved shear band, has been demonstrated many times in wavecode simulations of micromechanical problems, in which use of submicron elements was practicable (e.g., Zhu and Batra 1991). However, the practical use of submicron elements in macroscopic penetration calculations does not appear imminent, although the adaptive meshing approach (e.g., Camacho and Ortiz 1997) is progressing toward that goal. Moreover, the spatial resolution of shear bands would introduce formidable difficulties: extrapolations of the flow law and void model in terms of temperature, strain, and strain rate; possible phase change modeling; and the influence of practically unknowable microstructural features (e.g., individual inclusions and voids) that can trigger shear band nucleation.

2 The Model

2.1 Overview

The shear banding model is shown in Figure 1. This model is applied at the level of an individual finite element. P_{fail} and the ratio Y/Y_{JC} are each a function of ε^p. Here, Y is the imposed flow stress, P_{fail} is the imposed spall pressure, Y_{JC} is the flow stress as given by the Johnson-Cook strength model (Johnson and Cook 1983), and ε^p is the von Mises equivalent (effective) plastic strain, defined in terms of ϵ^p_{ij}, Cartesian components of the plastic strain tensor, by

$$d\varepsilon^p \;=\; \sqrt{\frac{2}{3}\, d\epsilon^p_{ij}\, d\epsilon^p_{ij}}\,. \tag{2}$$

Similarly, Y is applied to the von Mises equivalent stress, defined by

$$\bar{\sigma} \;=\; \sqrt{\frac{3}{2}\, \sigma'_{ij}\, \sigma'_{ij}}\,, \tag{3}$$

where σ'_{ij} are Cartesian components of the deviatoric Cauchy stress tensor (Malvern 1969b). The instability strain, ε^p_{inst}, is computed as a function of equivalent plastic strain rate, $\dot{\varepsilon}^p$, and temperature, θ. User-provided material constants include the pre-shear-banded spall pressure, $P^{(o)}_{fail}$, the ε^p-increment between initial instability and the beginning of localization, $\Delta\varepsilon^p_{loc}$, and the ε^p-increment between the beginning of localization and the attainment of a fully formed shear band, $\Delta\varepsilon^p_{fail}$. The other user-provided material parameters, b and $P^{(sb)}_{fail}$, involve the values attained by Y/Y_{JC} and P_{fail}, respectively, that characterize the fully formed shear band. b and $P^{(sb)}_{fail}$ are both functions of P_{loc}, the pressure at the beginning of localization. The two other quantities appearing in Figure 1 are the localization strain, ε^p_{loc}, and the failure strain, ε^p_{fail}, defined by

$$\varepsilon^p_{loc} \;=\; \varepsilon^p_{inst} + \Delta\varepsilon^p_{loc}\,, \tag{4}$$

$$\varepsilon^p_{fail} \;=\; \varepsilon^p_{inst} + \Delta\varepsilon^p_{loc} + \Delta\varepsilon^p_{fail}\,. \tag{5}$$

The features of the model are described and motivated in the remainder of §2.

2.2 Instability Strain

Bai (1982) studied analytically the growth of an infinitesimal perturbation to a constant-strain-rate simple shearing motion of a viscoplastic solid. He found an approximate condition for perturbation growth to be strain in excess of the level corresponding to maximum stress on the applicable constant-strain-rate adiabatic stress-strain curve (Figure 2). This critical strain is identified with ε^p_{inst} in the shear banding model.

Evaluation of ε^p_{inst} for a specific flow law proceeds as follows. Consider a flow law of the form

$$Y = Y(\varepsilon^p, \dot{\varepsilon}^p, \theta)\,. \tag{6}$$

Differential dY along a general thermodynamic path satisfies

$$dY = \frac{\partial Y}{\partial \varepsilon^p}\, d\varepsilon^p + \frac{\partial Y}{\partial \dot{\varepsilon}^p}\, d\dot{\varepsilon}^p + \frac{\partial Y}{\partial \theta}\, d\theta\,. \tag{7}$$

If, during time increment dt, the process is adiabatic and involves nonzero plastic strain increments (loading), and elastic strain increments are negligible, then $d\theta$ and $d\varepsilon^p$ are related by

$$\rho c \, d\theta = \beta Y d\varepsilon^p \ . \tag{8}$$

β is the fraction of plastic work that is converted to temperature rise, equal to about 0.9 for steel (Taylor and Quinney 1934).[1] For such an adiabatic process,

$$(dY)_{\text{adiabatic}} = \left(\frac{\partial Y}{\partial \varepsilon^p} + \frac{\beta Y}{\rho c} \frac{\partial Y}{\partial \theta} \right) d\varepsilon^p + \frac{\partial Y}{\partial \dot{\varepsilon}^p} d\dot{\varepsilon}^p \ . \tag{9}$$

If the adiabatic process also involves a constant strain rate ($d\dot{\varepsilon}^p = 0$), then

$$\left(\frac{dY}{d\varepsilon^p} \right)_{\substack{\text{adiabatic} \\ \dot{\varepsilon}^p = \text{const.}}} = \frac{\partial Y}{\partial \varepsilon^p} + \frac{\beta Y}{\rho c} \frac{\partial Y}{\partial \theta} \ . \tag{10}$$

The maximum stress on this constant-strain-rate adiabatic stress-strain curve occurs when

$$\frac{\partial Y}{\partial \varepsilon^p} + \frac{\beta Y}{\rho c} \frac{\partial Y}{\partial \theta} = 0 \ . \tag{11}$$

In the case of the Johnson-Cook flow law (Johnson and Cook 1983),

$$Y_{JC}(\varepsilon^p, \dot{\varepsilon}^p, \theta) \;=\; \left[A \,+\, B\,(\varepsilon^p)^N \right] \left[1 \,+\, C\, \ln \left(\frac{\dot{\varepsilon}^p}{1.0\ \text{s}^{-1}} \right) \right] \left[1 \,-\, \left(\frac{\theta - \theta_r}{\theta_m - \theta_r} \right)^M \right] , \tag{12}$$

where A, B, C, M, N, and θ_m are material constants, θ_m has the physical interpretation of melt temperature, and θ_r is the room temperature. Evaluation of $\partial Y_{JC}/\partial \varepsilon^p$ and $\partial Y_{JC}/\partial \theta$ and substitution into equation (11) yields the nonlinear algebraic equation for ε^p_{inst},

$$(\varepsilon^p_{inst})^{2N} + \frac{2A}{B} (\varepsilon^p_{inst})^N - F(\rho, \dot{\varepsilon}^p, \theta) (\varepsilon^p_{inst})^{N-1} + \left(\frac{A}{B} \right)^2 = 0 \ , \tag{13}$$

where

$$F(\rho, \dot{\varepsilon}^p, \theta) = \frac{\rho c N (\theta_m - \theta_r)}{\beta B M \left[1 + C \ln \left(\frac{\dot{\varepsilon}^p}{1.0\,\text{s}^{-1}} \right) \right] \left(\frac{\theta - \theta_r}{\theta_m - \theta_r} \right)^{M-1}} \ . \tag{14}$$

Equation (13) is solved for ε^p_{inst} by numerical iteration at every time step in each finite element that has not already satisfied the condition. Note that determination of ε^p_{inst} makes use of material parameters already introduced by the flow law and requires no additional parameters. Corresponding to the 4340 steel values for A, B, C, N, M, ρ, c, and θ_m published in Johnson and Cook (1983), values for ε^p_{inst} tend to range between 0.4 and 0.6, depending on strain rate and temperature.

This technique for evaluating ε^p_{inst} raises some issues: The conditions of constant strain rate and simple shear will not generally apply in a finite element throughout a penetration calculation. A finite amplitude perturbation could cause instability at a smaller strain (see Batra 1987). Pressure effects are neglected in the Johnson-Cook strength model. The application of von Mises plasticity in the definitions of ε^p and $\bar{\sigma}$ introduces the assumptions of initial material isotropy and subsequent isotropic hardening (Malvern 1969a).

[1] Note that temperature contributions from elastic strain are not assumed negligible throughout the problem, only during the increment of instability. Thus, θ remains the true temperature, with contributions from both plastic work and elastic strain energy.

2.3 Localization Strain and Failure Strain

Marchand and Duffy (1988) performed torsional Kolsky bar tests on thin-walled cylinders of HY-100 steel. Their dynamic torsional stress-strain curve from a test performed at room temperature and at a shear-strain rate of 1600 s^{-1} is shown in Figure 3. On this curve, maximum shear stress corresponds to a shear strain of about 0.27, or an effective strain of 0.31, somewhat smaller than the range of values typically obtained for ε^p_{inst} by the solution of equation (13) with the 4340 material constants published in Johnson and Cook (1983). This discrepancy may be attributable to material differences between HY-100 and 4340, and also to finite amplitude perturbations in the Marchand and Duffy experiments. Such finite amplitude perturbations may have originated from material microstructure, but also spuriously from geometric imperfections in the walls of the torsion specimen. The possible influence of geometric imperfections was noted in Marchand and Duffy (1988), but no measurement of surface variations was provided. If such measurements of surface imperfections were available, the analysis by Molinari and Clifton (1987) could be used to estimate the degree to which ε^p_{inst}, ε^p_{loc}, and ε^p_{fail} were shifted to smaller values.

In Figure 3, the localization shear strain, at which shear stress begins to decrease significantly, is roughly 0.38, which corresponds to an equivalent strain of 0.44. Hence, an estimate for $\Delta\varepsilon^p_{loc}$ is $0.44 - 0.31 = 0.13$.

In Figure 3, once localization is exceeded, the axis label of "*nominal* shear strain" is pertinent. A grid on the outer wall of the specimen was used to measure strain near the shear band, but a more local strain measurement within the band was not obtained. The figure shows that by a nominal shear strain of about 0.57, the stress is near zero and has effectively ceased to decrease. The corresponding equivalent strain is 0.66, which leads to an estimate for $\Delta\varepsilon^p_{fail}$ of $0.66 - 0.44 = 0.22$. Since the strain measurement was not ideally local, this $\Delta\varepsilon^p_{fail}$ estimate is a lower bound.

Further torsional Kolsky bar testing may reveal $\Delta\varepsilon^p_{loc}$ and $\Delta\varepsilon^p_{fail}$ to be significantly dependent on $\dot{\varepsilon}$, θ, and P. In the absence of such data, they are here treated as material constants. However, since ε^p_{inst} is a function of $\dot{\varepsilon}$ and θ, ε^p_{loc} and ε^p_{fail} will also vary with $\dot{\varepsilon}$ and θ according to equations (4) and (5).

In a followup to Marchand and Duffy (1988), Cho, Chi, and Duffy (1990) studied the mechanism of strength reduction to zero within a shear band in three different steels, including AISI 4340 with RHC 44, which is reasonably similar to RHA. (RHA has less carbon and an RHC of about 30.) They performed fractography on cracks within shear bands generated in torsional Kolsky bar specimens. In the case of RC-44 4340, cracking within the shear bands was associated with the coalescence of ductile voids that nucleated at debonding sites between the steel matrix and carbide inclusions. The debonding and subsequent growth of the voids were driven by the massive shear flow within the band. This indicates that in a torsion test, in which a state of simple shear is closely approximated, strength loss within a shear band has two contributions: (1) thermal softening and (2) microcracking associated with ductile voids.

2.4 Pressure-Dependent Residual Strength

In a penetration situation, a compressive shock wave is generated in both target and penetrator upon impact. If, for example, a tungsten-heavy-alloy rod impacts an RHA target at 1.5 km/s, the shock pressure in the target is roughly 64 GPa,[2] or an order of magnitude larger than the RHA flow stress of 1 to 2 GPa and spall stress of about 6 GPa (Bless 1981). This large superimposed compression is a feature not present in the torsion tests of Marchand and Duffy (1988) and Cho, Chi, and Duffy (1990).

The modified torsional Kolsky bar tests of Chichili and Ramesh (Chichili 1997; Chichili, Ramesh, and Hemker 1998; Chichili and Ramesh 1999) shed light on effects of pressure upon shear banding. In these tests, which involved alpha-titanium, an axial compression wave was applied prior to arrival of the torsional wave. The specimens were relatively thick-walled, as needed to prevent buckling under the compressive loading, and contained an axisymmetric notch on their outer wall. Near the notch tip, a finite element analysis showed the stress state to be approximated by simple shear plus hydrostatic stress. Chichili and Ramesh found that without superimposed pressure, the torsion produced intra-shear-band cracking associated with void nucleation and growth along grain boundaries. The application of compressive hydrostatic stresses on the order of the flow stress were able to suppress this cracking within the shear band, thereby allowing for some residual strength. This ability to suppress total strength loss by means of pressure reinforces the conclusion arrived at based on Cho, Chi, and Duffy (1990), namely, that the flow stress reduction observed by Marchand and Duffy and displayed in Figure 3 had two distinct contributions: thermal softening and ductile voids.

The feature of pressure-dependent residual strength is represented in the model by the function $b(P_{loc})$, given by

$$b(P_{loc}) \;=\; \begin{cases} 0 & ; P_{loc} \leq 0 \\ b_o \in [0,1] & ; P_{loc} > 0 \end{cases} \quad . \tag{15}$$

The user-provided material constant b_o introduces the assumption that for $\varepsilon^p > \varepsilon^p_{fail}$, strain hardening in the fully formed shear band follows the Johnson-Cook strength model, but with amplitudes of deviatoric stress components reduced by the factor b_o.

2.5 Spall Strength Reduction

When a projectile impacts a target, stress waves are generated in both materials. The target stress wave reflects upon impact with the rear surface to form a tensile wave. Simultaneously, unloading waves form along the penetration-hole boundary as new free surface is generated. These unloading waves interact with the reflected wave to form regions of large tensile stress, which can exceed the material's spall strength. (Recall that, in the case of a tungsten rod striking RHA, the initial shock pressure exceeds the RHA spall stress by an order of magnitude in terms of absolute value.) Hence, the phenomenon of spallation, or dynamic failure attributeable to tensile waves, can occur in the target.

[2]This estimate was obtained from the relationship $P_{shock} = \rho_o v_{shock} v_s$, where P_{shock} is shock pressure, ρ_o is undeformed RHA density, or about 7800 kg/m^3 (Johnson and Cook 1983), v_{shock} is longitudinal wave speed in RHA, or about 5.5 km/s, and v_s is the striking speed.

Bless (1981) measured spall stress, σ_{fail}, in RHA by plate-on-plate impact tests and reported the value of 6.0 GPa. (Note that σ_{fail} is an axial stress, not a von Mises equivalent stress.) Since the growth of a spherical ductile void is generally modeled to be driven by pressure (e.g., Rajendran, Dietenberger, and Grove 1989), in the shear banding model the spallation criterion is in terms of pressure. For the uniaxial strain condition of plate-on-plate impact tests, pressure and axial stress are related by (see Raftenberg 1996b)

$$\sigma_{fail} + P_{fail} = \frac{4Y}{3} . \tag{16}$$

Table 1 presents spall pressure, P_{fail}, for several reasonable values of flow stress. In the model, these values are applied to $P^{(o)}_{fail}$, the spall pressure of pre-shear-banded material. Data on the effects of pulse duration on spall stress are not available for RHA, so $P^{(o)}_{fail}$ is taken to be a negative-valued material constant, independent of loading rate.

Table 1: Estimates of $P^{(o)}_{fail}$ for RHA Corresponding to Reasonable Values of Y

Y (GPa)	P_{fail} (GPa)
1.0	−4.7
1.5	−4.0
2.0	−3.3
2.5	−2.7

There is compelling evidence that shear banding locally increases (or, in terms of absolute value, reduces) spall pressure. Irwin (1972) observed in penetrators composed of a U-2Mo alloy that ductile voids formed selectively within shear bands (Figure 4). The equiaxed nature of the voids in this figure strongly suggests that they grew under the influence of hydrostatic tension, or negative pressure. The tensile wave was evidently able to grow voids within the shear band, but not in the adjacent material outside the band. This phenomenon of spall pressure increase within a shear band is introduced into the model by the function $P^{(sb)}_{fail}(P_{loc})$, which satisfies the relation

$$P^{(o)}_{fail} \leq P^{(sb)}_{fail}(P_{loc}) < 0 \quad \forall \, P_{loc} . \tag{17}$$

There are presumably two mechanisms contributing to spall pressure increase within shear bands, in close analogy with the two proposed contributions to flow stress reduction. First, spall pressure is increased by any void nucleation and growth that occurred during shear band formation. Second, thermal softening lowers resistance to void growth, thereby increasing spall pressure. The first contribution would again presumably be eliminated by the presence of a sufficiently large positive pressure during the process of shear band formation. Hence, a distinction is introduced between $P^{(sb-)}_{fail}$ and $P^{(sb+)}_{fail}$, two user-provided material constants defined by

$$P^{(sb)}_{fail}(P_{loc}) = \begin{cases} P^{(sb-)}_{fail} & ; P_{loc} \leq 0 \\ P^{(sb+)}_{fail} & ; P_{loc} > 0 \end{cases} , \tag{18}$$

where

$$P_{fail}^{(o)} \leq P_{fail}^{(sb-)} \leq P_{fail}^{(sb+)} < 0\,. \tag{19}$$

That is, if shear banding formed under compression, spall pressure is increased (or decreased in terms of absolute value) from $P_{fail}^{(o)}$ by a lesser or equal amount than if shear banding formed under tension.

Once the condition $P \leq P_{fail}(\varepsilon^p, P_{loc})$ is satisfied, that element can no longer support deviatoric stresses or hydrostatic tension.

3 An Application

3.1 Description of Problems

In 1993–94, ARL performed a series of tests in each of which an RHA plate of either 50.8- or 76.2-mm thickness was perforated by a small-L_s/D_s right circular cylinder composed of 91W-6Ni-3Co tungsten heavy alloy (WHA), which impacted at normal incidence (Raftenberg and Kennedy 1995). The six problems that were studied are described in Table 2; v_s, L_s, and D_s are the striking speed, length, and diameter, respectively, of the WHA rod, and d is the thickness of the RHA target, a circular plate with a 1-m diameter. The rear of the rod was surrounded by a stabilizing 7075–T651 aluminum drag flare in the form of a truncated cone. A total of 10 experiments were performed (Table 3). In each, the impact speed was within 100 m/s of the desired value, and the impact obliquity, γ_s, was 3.00 degrees or less. The experiments are more thoroughly described in Raftenberg and Kennedy (1995).

Table 2: Six Problems Defined

Problem	v_s (mm/μs)	L_s (mm)	D_s (mm)	d (mm)
1	1.52	112.0	20.9	50.8
2	1.90	92.0	18.3	50.8
3	2.30	65.0	16.3	50.8
4	1.52	112.0	20.9	76.2
5	1.90	92.0	18.3	76.2
6	2.30	65.0	16.3	76.2

3.2 Description of the Computations

The six problems were simulated with the EPIC lagrangian wavecode (Johnson and Stryk 1992), into which the shear banding model had been installed. All finite elements were axisymmetric three-node triangles arranged in rectangular groups of four crossed-triangles. There were 5 such rectangles across the radius of the rod and 50 along the length. For the 50.8-mm-thick targets, there were 25 such rectangles across the thickness and 200 across the radius. For the 76.2-mm-thick targets, there were 38 such rectangles across the thickness

Table 3: Ten Experiments Identified

Test No.	v_s (mm/μs)	L_s (mm)	D_s (mm)	γ_s (deg)	d (mm)	Problem
1086	1.57	112.0	20.9	0.40	50.8	1
1071	1.84	92.0	18.3	3.00	50.8	2
1089	1.93	92.0	18.3	2.54	50.8	2
1069	2.30	65.0	16.3	2.33	50.8	3
1087	1.59	112.0	20.9	2.24	76.2	4
1076	1.62	112.0	20.9	0.90	76.2	4
1090	1.91	92.0	18.3	1.18	76.2	5
1075	1.99	92.0	18.3	1.56	76.2	5
1092	2.26	65.0	16.3	2.22	76.2	6

and 200 across the radius. Eroding slidelines (Johnson and Stryk 1996) were located at the interfaces between rod and target, rod and flare, and flare and target; an erosion strain of 1.5 and a Coulombic friction coefficient of zero were used throughout.

The shear banding model was applied to the RHA target material in all calculations, with the parameters $P_{fail}^{(o)}$ set to -3.0 GPa (based on Table 1), $\Delta\varepsilon_{loc}^{p}$ to 0.13, and $\Delta\varepsilon_{fail}^{p}$ to 0.22 (the last two based on Figure 3). $P_{fail}^{(sb+)}$ and $P_{fail}^{(sb-)}$ were always equated (hence, the symbol $P_{fail}^{(sb)}$ is used as replacement), and their shared value was varied in the range between -3.0 and -0.2 GPa. b_o was varied between 0.0, 0.5, and 1.0. Note that $b_o = 0.0$ is the special case when the fully formed shear band has no residual strength. $b_o = 1.0$ is the case when Y_{JC} is applied to the fully formed shear band (except in the rare occasion that $P_{loc} \leq 0$), so that the shear banding model degenerates to spall pressure increase only.

For the WHA rod material and the aluminum of the flare, the Johnson-Cook fracture model (Johnson and Cook 1985) was used to represent damage. This model introduces the seven material constants D_1, D_2, D_3, D_4, D_5, ε_{min}^{f}, and σ_{spall}. These were assigned the values in Table 4, which were obtained from Johnson (1997) for 7039 Al and 90W–7Ni–3Fe.

The Johnson-Cook strength model was used to evaluate flow stress, Y_{JC}, for RHA, WHA, and Al. The von Mises plasticity algorithm imposed isotropic hardening. Elastic deviatoric strains were related to deviatoric stresses by the elastic shear modulus, G, assumed to be a material constant. G and the Johnson-Cook-strength constants A, B, C, M, N, and θ_m were assigned the values from Johnson and Cook (1983) that are listed in Table 4. The values given in Johnson and Cook (1983) for Rockwell C-30, austenitized, quenched, and tempered 4340 steel were assigned to RHA. Those given for 90W–7Ni–3Fe were assigned to the 91W–6Ni–3Co WHA, and those for 7039 Al were assigned to the 7075-T651 Al.

Dilatation of the three metals was governed by the Mie-Grüneison equation of state, with the shock-Hugoniot pressure, P_H, related to compression, μ, by the cubic

$$P_H(\mu) = K_1\mu + K_2\mu^2 + K_3\mu^3 \,, \tag{20}$$

where

$$\mu = \frac{\rho - \rho_o}{\rho_o} \,. \tag{21}$$

Table 4: Material-Constant Values

Material Constant	Al	WHA	RHA
ρ_o (kg/m^3)	2768.	17000.	7830.
K_1 (GPa)	76.74	246.1	163.9
K_2 (GPa)	128.3	391.9	294.4
K_3 (GPa)	125.1	820.8	500.0
Γ	2.00	1.43	1.16
G (GPa)	26.20	124.11	77.50
A (GPa)	0.3365	1.5058	0.7922
B (GPa)	0.3427	0.1765	0.5095
C	0.010	0.016	0.014
M	0.41	0.12	0.26
N	1.00	1.00	1.03
θ_r (K)	294.3	294.3	294.3
θ_m (K)	877.6	1723.2	1793.2
c (J/kg-K)	875.6	134.5	477.8
D_1	0.14	0.0	—
D_2	0.14	0.33	—
D_3	−1.5	−1.5	—
D_4	0.018	0.000	—
D_5	0.00	0.00	—
ε^f_{min}	0.060	0.022	—
σ_{spall} (GPa)	4.62	6.76	—
$P^{(o)}_{fail}$ (GPa)	—	—	−3.00
$\Delta\varepsilon^p_{loc}$	—	—	0.13
$\Delta\varepsilon^p_{fail}$	—	—	0.22

ρ is the current density, and ρ_o is the undeformed density. K_1, K_2, and K_3 are material constants, as is the Grüneison coefficient, Γ. Values assigned to these constants and to ρ_o are listed in Table 4. For aluminum, ρ_o was obtained from Johnson and Cook (1983) for 2024-T351 Al; and K_1, K_2, K_3, and Γ were obtained from Kohn (1969) for 2024 Al. For RHA, ρ_o was obtained from Johnson and Cook (1983) for 4340 steel. K_1, K_2, K_3, and Γ were obtained from Kohn (1969) for 304 stainless steel. For WHA, ρ_o was obtained from Johnson and Cook (1983) for a 90W–7Ni–3Fe alloy. Γ was assigned the value in Kohn (1969) for pure tungsten, while K_1, K_2, and K_3 were evaluated from the linear shock speed-particle speed curve reported in Hauver (1980) for 90W–7Ni–3Fe.

3.3 Computational and Experimental Results Compared

After each experiment, the target plate was sectioned along an approximate perforation-hole diameter to reveal hole morphology and locations of cracks and cavities. Figure 5 shows the sectioned plate from Test 1071. Note the cracks that enter the plate from the hole boundary. Also note the "spall ring shelf" that surrounds the hole boundary at the exit surface. This feature was created by the separation from the plate of the largest fragments that were observed. For each plate, the hole boundary, spall ring shelf, cracks emanating from the hole boundary, and internal cavities were digitized. These digitizations in the case of Test 1086 are shown in Figure 6. From the hole boundary digitization, the through-thickness-averaged hole diameter, $\overline{D}$, was computed by integrating from the initial elevation of the entrance surface, $z = 0$, to that of the exit surface, $z = -50.8$ mm or -76.2 mm. Note that this integration did not include contributions from the spall ring shelf region since the lip of the overhang crossed the initial elevation of the exit surface. An uncertainty in the experimental $\overline{D}$ value of about ± 0.3 mm was introduced by the boundary digitization procedure. Additional uncertainties introduced by deviations from the intended impact speed and small unintended yaw angles are difficult to quantify. Flash radiography was used to measure the length, L_{res}, and speed, v_{res}, of the residual rod shortly after its emergence from the target exit surface.

All EPIC simulations were run for 2.5 ms after initial impact at time $t = 0$. The quantites $\overline{D}$, L_{res}, and v_{res} were computed from each EPIC simulation at 2.5 ms.

Figures 7 through 12 plot $\overline{D}$ vs. $P_{fail}^{(sb)}$ with b_o a parameter for each of the six problems. In each of these figures, the dashed line(s) indicate experimental measurements. The computational point $P_{fail}^{(sb)} = -3.0$ GPa, $b_o = 1.0$ is essentially the solution without the shear banding model. In each of Problems 1 through 5 (no $\overline{D}$ measurement was obtained for Problem 6), this point is significantly smaller than the measured values. In Problem 1, for instance, the computed $\overline{D}$ of 38.8 mm is 11.5% smaller than the experimental value of 43.6 mm, or roughly 23% smaller in terms of hole volume. Figure 13 plots $\overline{D}$ vs. v_s from the six problems for this case of $P_{fail}^{(sb)} = -3.0$ GPa, $b_o = 1.0$.

In Figures 7 through 12, for a given $P_{fail}^{(sb)} \leq -1.0$ GPa the computed $\overline{D}$ results exhibit the anticipated trend of increasing as b_o (the residual Y/Y_{JC} value within the fully formed shear band) decreases through the values 1.0, 0.5, 0.2, and 0.0. The $\overline{D}$ results for $b_o = 0.0$ and $b_o = 0.2$ are relatively insensitive to $P_{fail}^{(sb)}$ throughout the range $P_{fail}^{(sb)} \leq 0.0$. In Problems 2 and 4, for each of which there are two experimental measurements for $\overline{D}$, $b_o = 0.0$ results are close to the larger measurement, and $b_o = 0.2$ results are close to the smaller measurement. In

Problem 5, for which there are also two experimental measurements for $\overline{D}$, $b_o = 0.0$ results lie between the two measurements and the $b_o = 0.2$ results are slightly smaller than the smaller measurement. The scatter of 2 to 3 mm between the two experimental measurements in these figures can perhaps be attributed to variations in impact speed and yaw angle. In Problem 1, the $b_o = 0.0$ and $b_o = 0.2$ results lie above the single measurement, while in Problem 3 they lie below the single measurement. Throughout Problems 1 through 6, $\overline{D}$ results corresponding to $b_o = 0.5$ and $b_o = 1.0$ are rather insensitive to $P_{fail}^{(sb)}$ throughout the range $P_{fail}^{(sb)} \leq -1.0$ GPa, but then increase with increasing $P_{fail}^{(sb)}$ for $P_{fail}^{(sb)} > -1.0$ GPa. Throughout Problems 1 through 5, at $P_{fail}^{(sb)} = -0.2$ GPa the $\overline{D}$ results for $b_o = 0.0$ and $b_o = 0.5$ come reasonably close to one or more measured values.

Figure 14 plots L_{res} vs. $P_{fail}^{(sb)}$ with b_o a parameter for Problem 2. For a given problem, one or two measurements were obtained for L_{res}^{exp}, the experimental residual rod length, while 24 values were obtained for computational residual rod length, L_{res}^{comp}, corresponding to permutations of $P_{fail}^{(sb)} = -3.0, -2.0, -1.5, -1.0, -0.5, -0.2$ GPa and $b_o = 0.0, 0.2, 0.5, 1.0$. $L_{res}^{|comp-exp|}$ is defined to be the maximum discrepancy between an L_{res}^{comp} value and a specific L_{res}^{exp}, so

$$L_{res}^{|comp-exp|} = \max_{\left(P_{fail}^{(sb)}, b_o\right)} |L_{res}^{comp} - L_{res}^{exp}| . \tag{22}$$

$L_{res}^{|comp-exp|}$ values from the nine experiments for which an x-ray flash allowed for the determination of L_{res}^{exp} are listed in Table 5. ΔL^{exp} is defined to be an experimentally measured net rod shortening,

$$\Delta L^{exp} = L_s - L_{res}^{exp} . \tag{23}$$

In Table 5 $L_{res}^{|comp-exp|}$ is normalized by ΔL^{exp}, and we see that the computational "error" in residual rod length varies between 4.1 and 18.7% of the net shortening. Hence, reasonably accurate results for rod shortening were obtained from all EPIC runs, including those for which the shear banding model was effectively inoperative ($P_{fail}^{(sb)} = -3.0$ GPa, $b_o = 1.0$).

Table 5: Comparison of Computational and Experimental L_{res} Results

Problem	L_s (mm)	L_{res}^{exp} (mm)	ΔL^{exp} (mm)	$L_{res}^{\|comp-exp\|}$ (mm)	$\frac{L_{res}^{\|comp-exp\|}}{\Delta L^{exp}}$ (%)
1	112.0	67.2	44.8	2.5	5.6
2	92.0	48.8	43.2	4.7	10.9
		46.0	46.0	3.3	7.2
3	65.0	23.4	41.6	6.1	14.7
4	112.0	49.3	62.7	2.6	4.1
		52.6	59.4	5.9	9.9
5	92.0	33.1	58.9	5.4	9.2
		34.0	58.0	6.3	10.9
6	65.0	16.3	48.7	9.1	18.7

Figure 15 plots v_{res} vs. $P_{fail}^{(sb)}$ for Problem 2. As shown in Tables 2 and 3, for some experiments there was considerable discrepancy between the achieved striking speed, v_s^{exp}, (measured with a streak camera) and the intended value. From each of the seven experiments for which two x-ray flashes allowed for a determination of residual speed, v_{res}^{exp}, an experimental net rod deceleration, Δv^{exp}, defined by

$$\Delta v^{exp} = v_s^{exp} - v_{res}^{exp} , \tag{24}$$

was determined (Table 6). For each problem, the striking speed in the EPIC simulations, v_s^{comp}, was of course the intended value, and corresponding to each of the 24 permutations of $(P_{fail}^{(sb)}, b_o)$, a residual speed, v_{res}^{comp}, was computated. The minimum and maximum results for rod deceleration, Δv_{min}^{comp} and Δv_{max}^{comp}, respectively, defined by

$$\Delta v_{max}^{comp} = \max_{\left(P_{fail}^{(sb)}, b_o\right)} \left(v_s^{comp} - v_{res}^{comp}\right) , \tag{25}$$

$$\Delta v_{min}^{comp} = \min_{\left(P_{fail}^{(sb)}, b_o\right)} \left(v_s^{comp} - v_{res}^{comp}\right) , \tag{26}$$

are also listed in Table 6. Comparison of Δv_{min}^{comp} and Δv_{max}^{comp} with Δv^{exp} in Problems 3 and 4 reveals that computational results for rod deceleration were significantly smaller than experimental results for these two problems. In Problem 1, computational decelerations agree with one of the two experiments but are smaller than results from the other. In Problem 5, computational decelerations are bounded by results from the two experiments.

Table 6: Comparison of Computational and Experimental v_{res} Results

Problem	v_s^{exp} (mm/μs)	v_{res}^{exp} (mm/μs)	Δv^{exp} (mm/μs)	v_s^{comp} (mm/μs)	Δv_{min}^{comp} (mm/μs)	Δv_{max}^{comp} (mm/μs)
1	1.57	—	—	1.52	0.12	0.14
2	1.84	1.63	0.21	1.90	0.15	0.19
	1.93	1.74	0.19			
3	2.30	1.94	0.36	2.30	0.22	0.32
4	1.59	1.29	0.30	1.52	0.22	0.26
	1.62	1.35	0.27			
5	1.91	1.58	0.33	1.90	0.25	0.32
	1.99	1.77	0.22			
6	2.26	—	—	2.30	0.45	0.67

Figures 6 and 16 through 20 show a time sequence of mesh plots from Problem 1 with $P_{fail}^{(sb)} = -0.2$ GPa and $b_o = 0.5$. The finite element meshes are superimposed over the digitizations of experimental hole profile and crack and cavity locations. The "Computational Damage" legend indicates the status of colored finite elements with regard to the shear banding model. Table 7 interprets legend entries in terms of the model. At 25 μs after impact (Figure 16), there are small regions of spalled RHA elements lining the perforation hole. Among the RHA elements that have not yet spalled, those closest to the hole satisfy the condition $\varepsilon_{fail}^p \leq \varepsilon^p$. Adjacent to these is a band of elements that satisfy $\varepsilon_{loc}^p \leq \varepsilon^p < \varepsilon_{fail}^p$, and these are followed by a band that satisfy $\varepsilon_{inst}^p \leq \varepsilon^p < \varepsilon_{loc}^p$. At 50 μs (Figure 17), there is a small region of RHA near the exit surface that has spalled, satisfying the condition $\varepsilon^p < \varepsilon^p_{inst}$; $P \leq P^{(o)}_{fail}$. Note in Figure 20 that reasonable agreement has been achieved in terms of $\overline{D}$, but the spall ring shelf is missing from the calculated result. Also, colored elements that have satisfied the instability condition do not extend as far radially into the targets as do the experimental cracks; each one of which presumably runs along a shear band (Raftenberg and Krause, 1999).

Table 7: Code for Damage Legend on Mesh Plots

Legend Entry	Interpretation	
NO INSTAB; SPALL	$\varepsilon^p < \varepsilon^p_{inst}$;	$P \leq P^{(o)}_{fail}$
INSTAB BUT NO LOC; NO SPALL	$\varepsilon^p_{inst} \leq \varepsilon^p < \varepsilon^p_{loc}$;	$P > P^{(o)}_{fail}$
INSTAB BUT NO LOC; SPALL	$\varepsilon^p_{inst} \leq \varepsilon^p < \varepsilon^p_{loc}$;	$P \leq P^{(o)}_{fail}$
LOC BUT NO FAILURE; NO SPALL	$\varepsilon^p_{loc} \leq \varepsilon^p < \varepsilon^p_{fail}$;	$P > P^{(o)}_{fail} + [P^{(sb)}_{fail} - P^{(o)}_{fail}]\left(\frac{\varepsilon^p - \varepsilon^p_{loc}}{\Delta\varepsilon^p_{fail}}\right)$
LOC BUT NO FAILURE; SPALL	$\varepsilon^p_{loc} \leq \varepsilon^p < \varepsilon^p_{fail}$;	$P \leq P^{(o)}_{fail} + [P^{(sb)}_{fail} - P^{(o)}_{fail}]\left(\frac{\varepsilon^p - \varepsilon^p_{loc}}{\Delta\varepsilon^p_{fail}}\right)$
FAILURE; NO SPALL	$\varepsilon^p_{fail} \leq \varepsilon^p$;	$P > P^{(sb)}_{fail}$
FAILURE; SPALL	$\varepsilon^p_{fail} \leq \varepsilon^p$;	$P \leq P^{(sb)}_{fail}$

Figures 21 through 23 present computational and experimental results from the six problems when $P^{(sb)}_{fail} = -0.2$ GPa, $b_o = 0.5$. Comparison of Figure 21 with Figure 13 shows that the shear banding model has allowed for improved agreement with experimental hole size while maintaining reasonable agreement with measured values for L_{res} and v_{res} (Figures 22 and 23).

4 Concluding Remarks

4.1 Summary of Results

A shear banding model was developed to impose on a finite element the effects of adiabatic shear. These are deemed to be reduction in the ratio of flow stress to the value predicted by the Johnson-Cook strength model and increase in spall pressure. The instability strain, ε^p_{inst}, is identified with the maximum on the constant-strain-rate, adiabatic stress-strain curve at the current level of strain rate. After a strain increment, $\Delta\varepsilon^p_{loc}$, the localization strain is reached, at which point the reduction in the flow stress ratio and the increase in spall pressure from its initial value of $P^{(o)}_{fail}$ both commence. This reduction and increase proceed as linear functions of equivalent plastic strain until a second strain increment, $\Delta\varepsilon^p_{fail}$, is achieved, at which point the flow stress ratio attains its residual value, $b(P_{loc})$, and the spall pressure attains its shear-banded value of $P^{(sb)}_{fail}$. $P^{(sb)}_{fail}$ was treated as a material constant, and $b(P_{loc})$ introduces another material constant, b_o.

$\Delta\varepsilon^p_{loc}$, $\Delta\varepsilon^p_{fail}$, and $P^{(o)}_{fail}$ were also treated as material constants. The first two were assigned values from a constant-strain-rate torsional Kolsky bar test on HY-100, and the third from a plate-on-plate impact test on RHA. $P^{(sb)}_{fail}$ and b_o are at present unevaluated and were treated as "free" parameters.

The model was installed into EPIC and applied to a set of six problems involving perforation of RHA plates by WHA rods. The model was found able to rectify an important shortcoming in previous calculations, namely, a sufficiently large target hole size was achieved, albeit by means of "free" parameters. The feature of the spall ring shelf at the target exit surface remains elusive.

4.2 Suggestions for Future Work

For the application of RHA plate perforation, evaluations of the model's parameters $\Delta\varepsilon^p_{loc}$ and $\Delta\varepsilon^p_{fail}$ can be refined by means of torsional Kolsky bar tests on RHA. The possible dependency of these parameters upon strain rate can also thereby be explored.

The currently unevaluated parameters $P^{(sb)}_{fail}$ and b_o have a clear physical significance and should in principle be amenable to experimental evaluation. The compression-torsion Kolsky bar (Chichili 1997; Chichili and Ramesh 1999) may provide a means for evaluating b_o during the compression phase of the experiment, when cracking within the shear band is suppressed. However, much uncertainty is introduced by the finite element calculation that is used to estimate residual stress within the shear band (Ramesh 1999). Using this same apparatus, perhaps by not trapping the compression wave a tensile wave can be subsequently delivered to the fully formed shear band with some controlled delay of arrival time, and evaluation of $P^{(sb)}_{fail}$ can thereby be investigated.

Kerley (1993) simulated by means of the Eulerian CTH code (McGlaun et al., 1990) an experiment conducted by Raftenberg (Raftenberg 1994), in which a 13-mm-thick RHA plate was perforated by a copper shaped charge jet. The simulation included the generally neglected phenomenon of the $\alpha \rightleftharpoons \epsilon$ iron phase transformation (Kerley 1993), and this feature was found crucial in obtaining an accurate hole morphology, particularly at the regions of the entrance and exit faces. (However, the calculation used perfect plasticity and contained no damage model, and so was simplistic in other regards.) The thin 13-mm-thick plate contained no true spall ring shelf in the simulations or experiment, but the calculations are nevertheless suggestive that for a thicker plate inclusion of the phase transformation representation may be what is needed to produce the shelf.

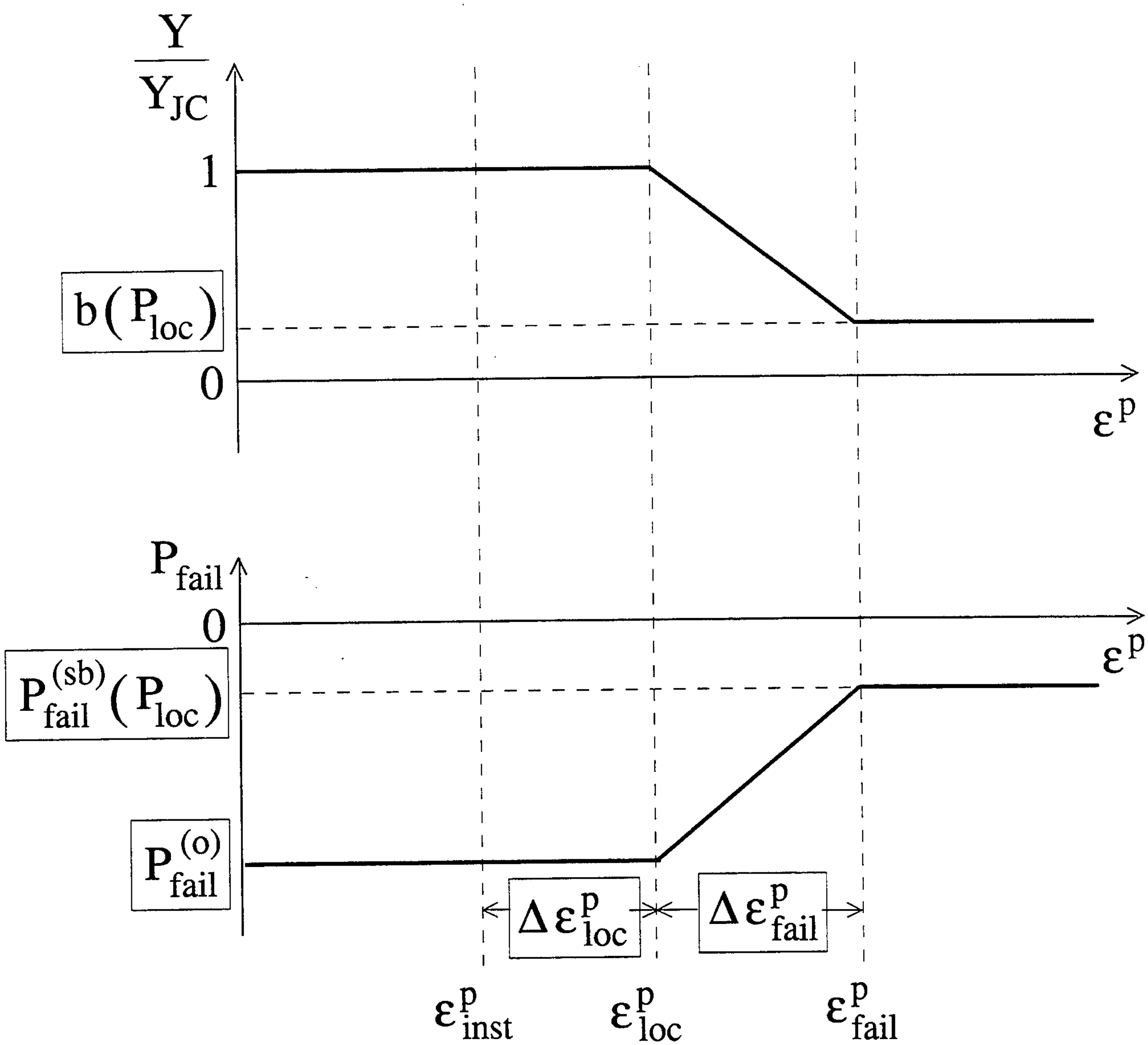

Figure 1: The Shear Banding Model. (The five boxed quantities are user-provided input to the model.)

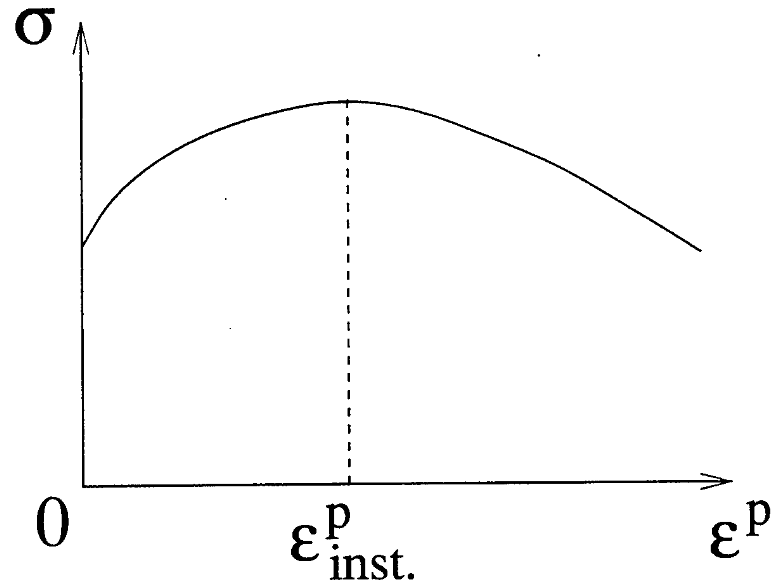

Figure 2: An Adiabatic Stress-Strain Curve at Constant Strain Rate.

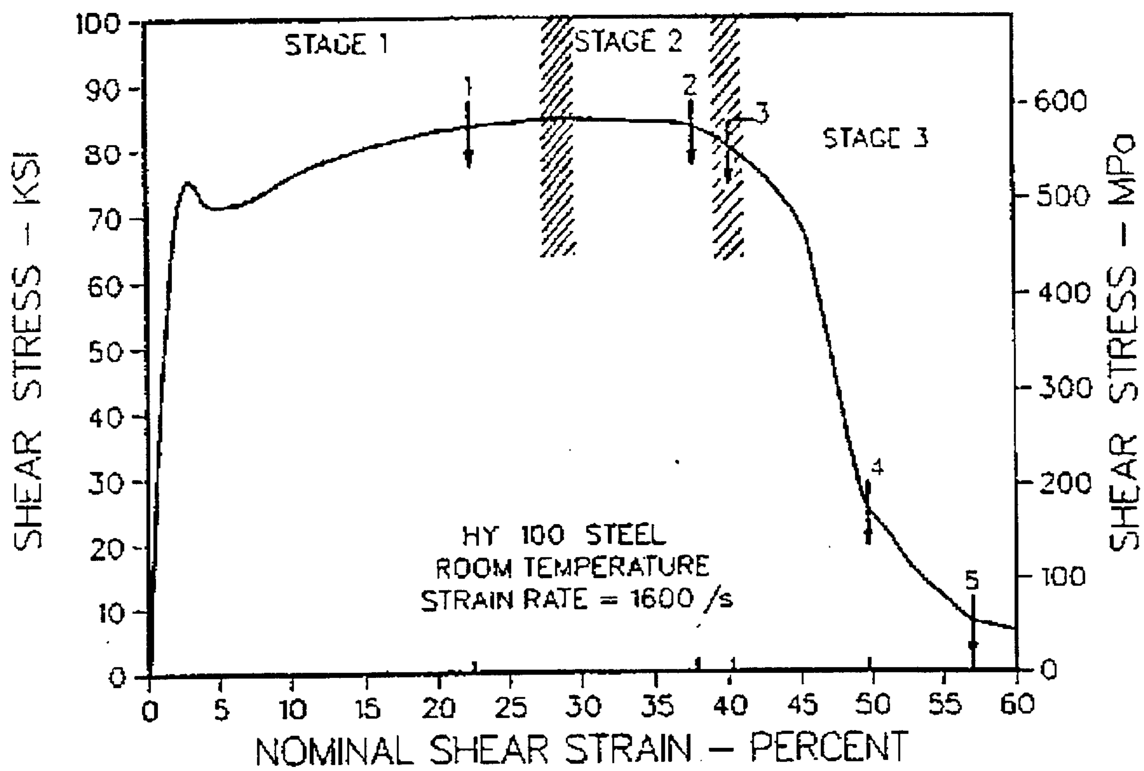

Figure 3: Torsional Stress-Strain Curve for HY-100 Steel at Room Temperature and a Constant Strain Rate of 1600 s^{-1} (reproduced from Marchand and Duffy [1988], Figure 12, with permission from the publisher).

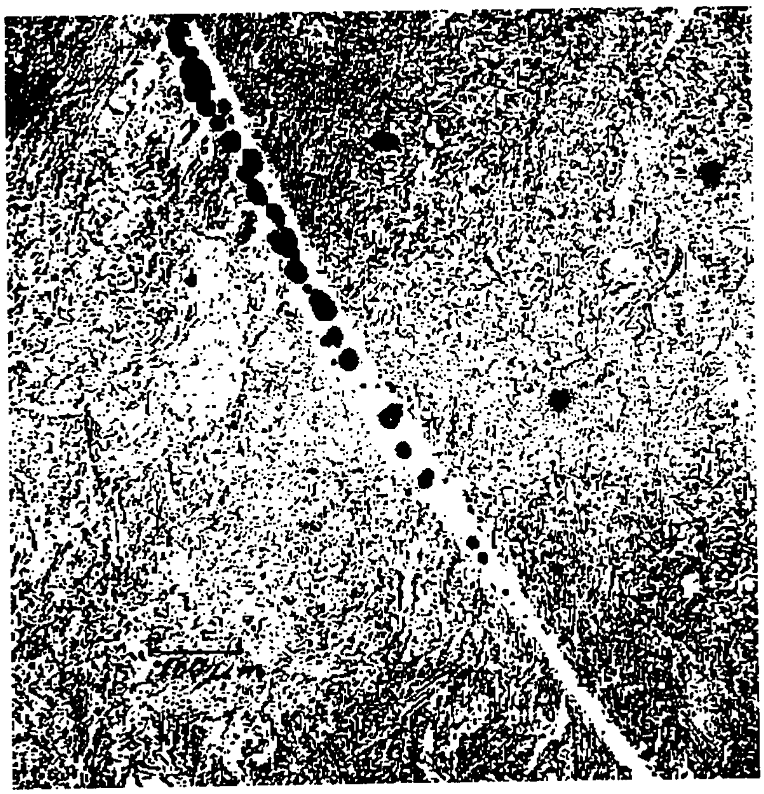

Figure 4: Ductile Voids Within a Shear Band in a U-2Mo Penetrator (reproduced from Irwin [1972] with permission from Defence Research Establishment Valcartier).

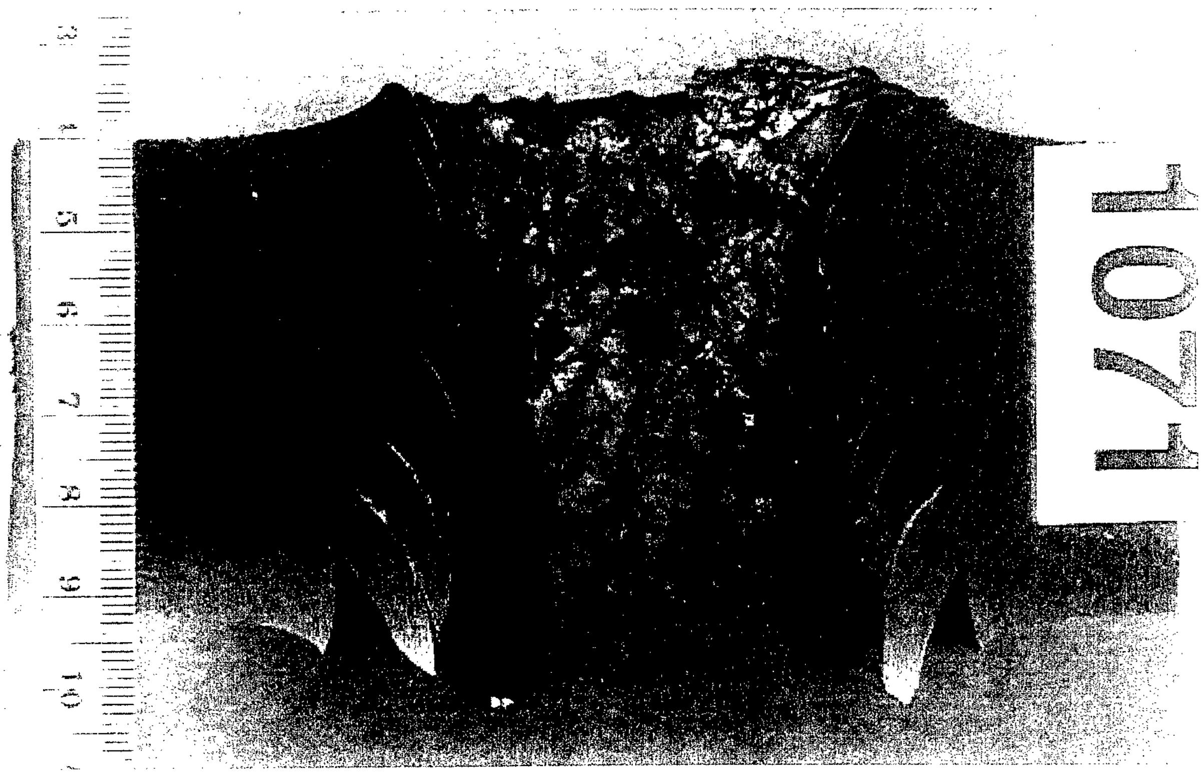

Figure 5: Sectioned Target Plate from Test 1071.

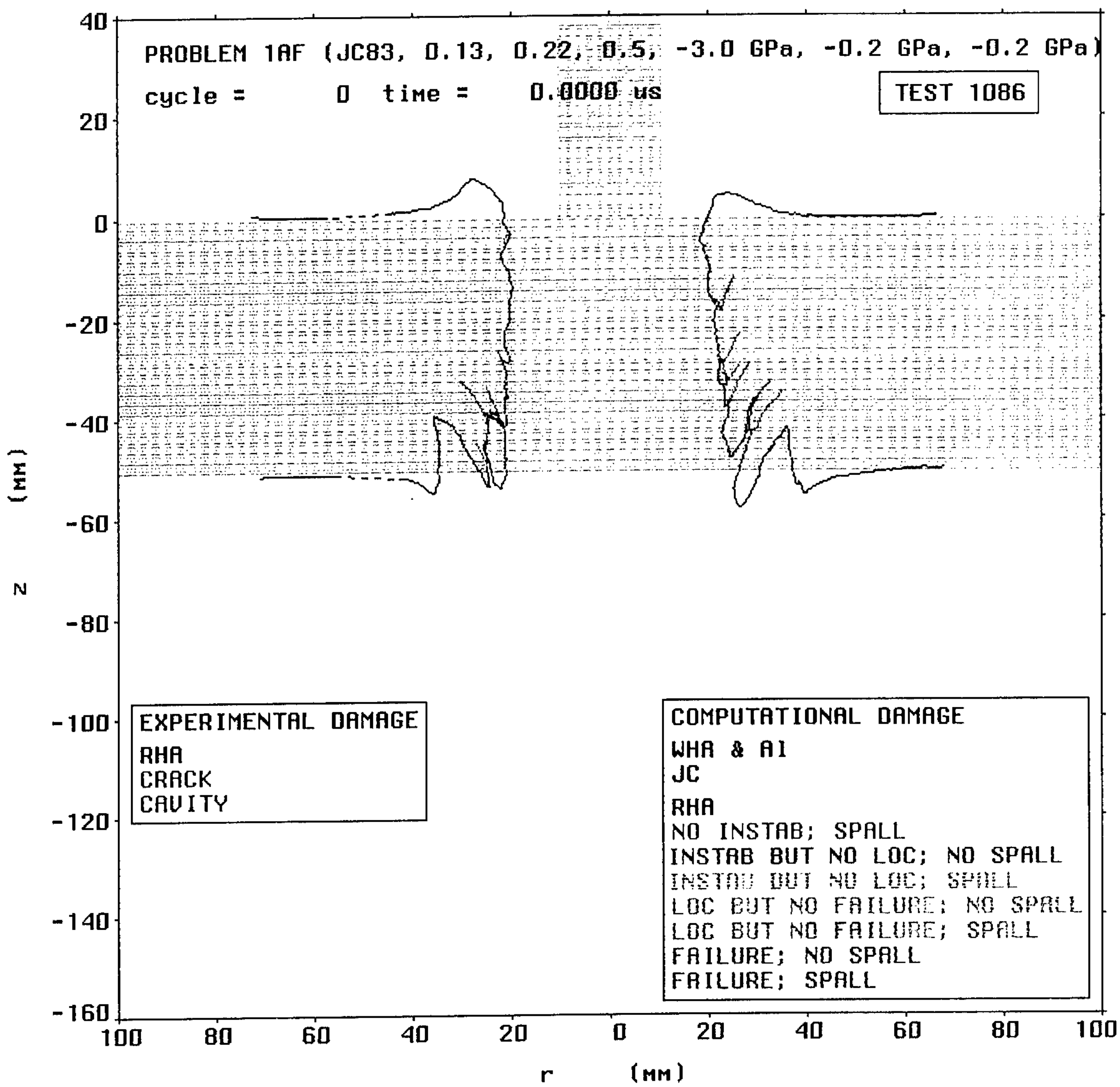

Figure 6: Initial Mesh for Problem 1, Superimposed on Digitized Experimental Perforation-Hole Contour With Cavities and Cracks Indicated.

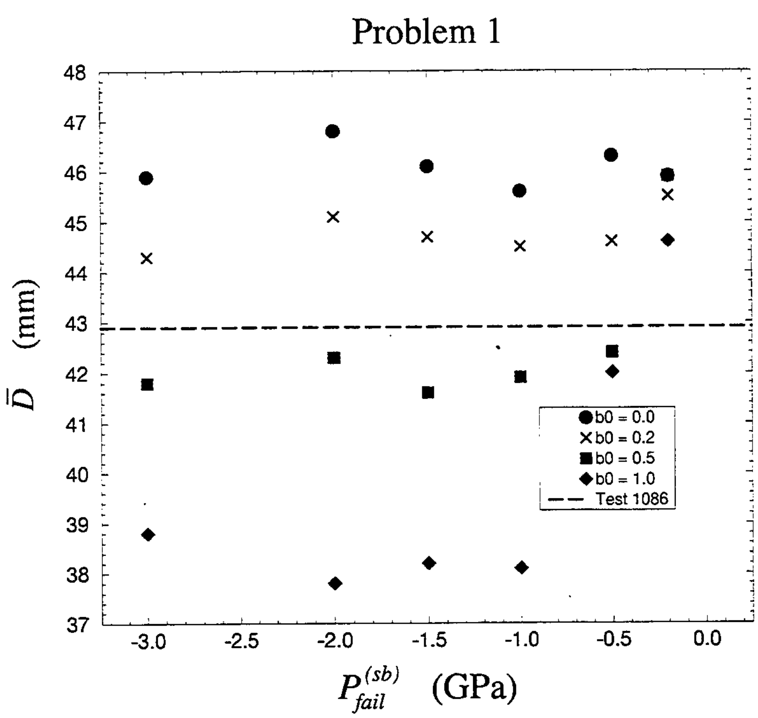

Figure 7: Final Through-Thickness-Averaged Hole Diameter vs. Spall Pressure of Shear-Banded RHA From Problem 1.

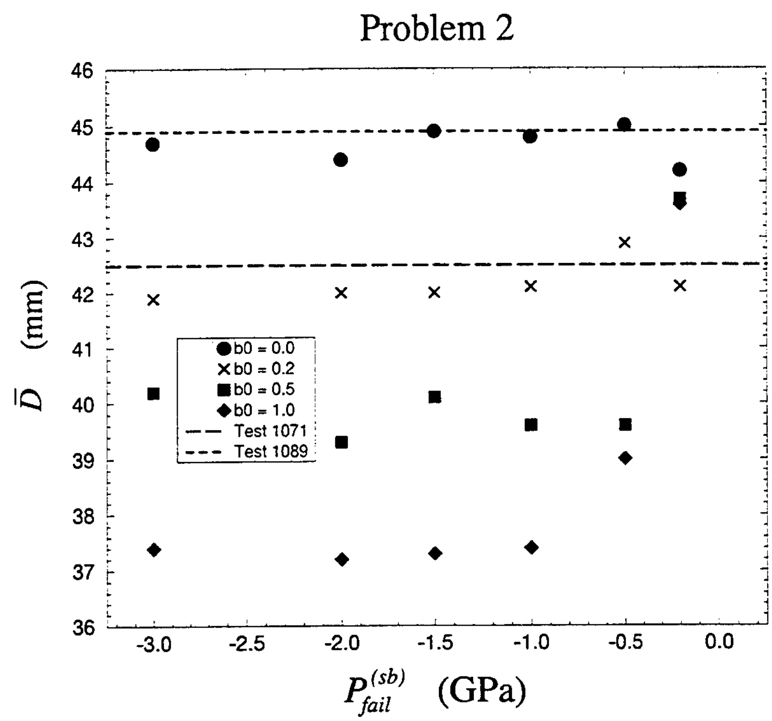

Figure 8: Final Through-Thickness-Averaged Hole Diameter vs. Spall Pressure of Shear-Banded RHA From Problem 2.

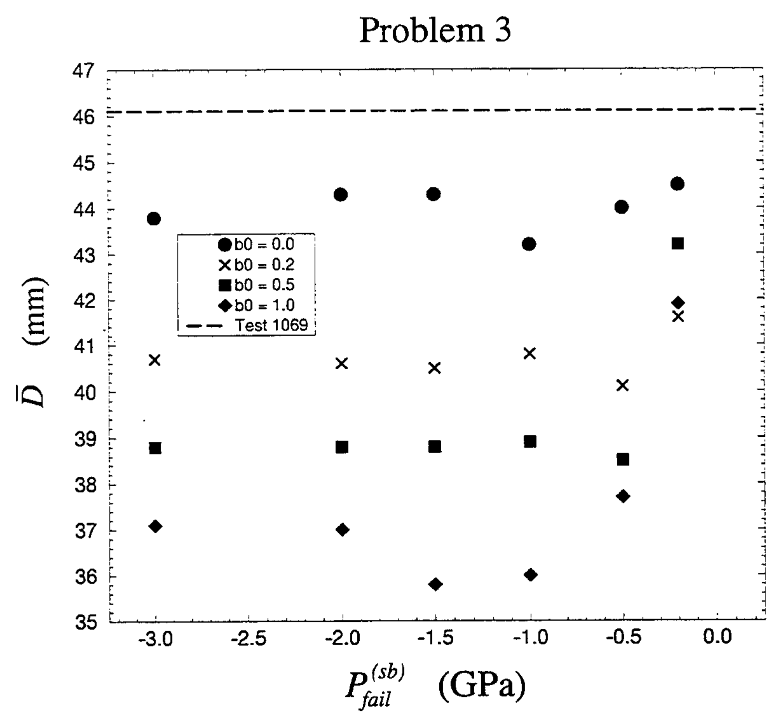

Figure 9: Final Through-Thickness-Averaged Hole Diameter vs. Spall Pressure of Shear-Banded RHA From Problem 3.

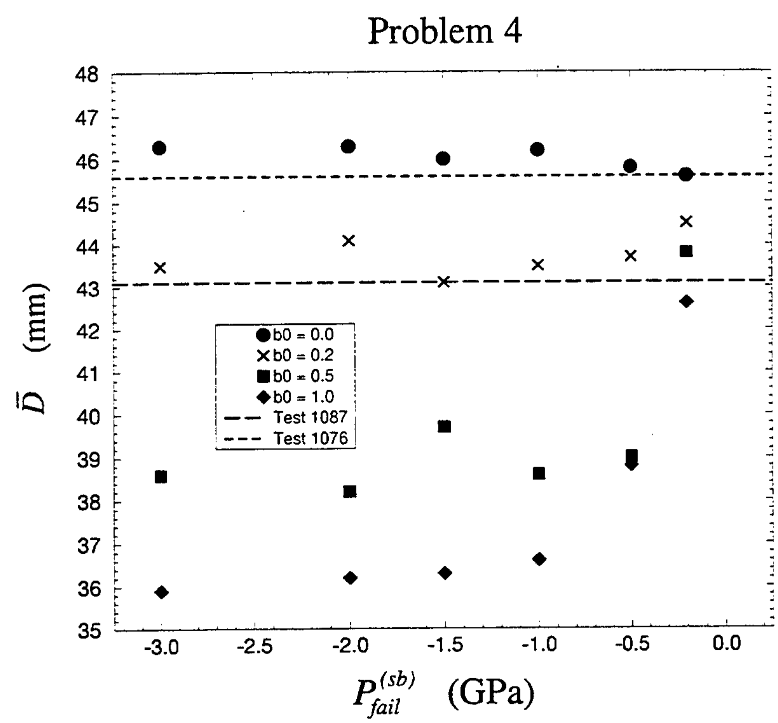

Figure 10: Final Through-Thickness-Averaged Hole Diameter vs. Spall Pressure of Shear-Banded RHA From Problem 4.

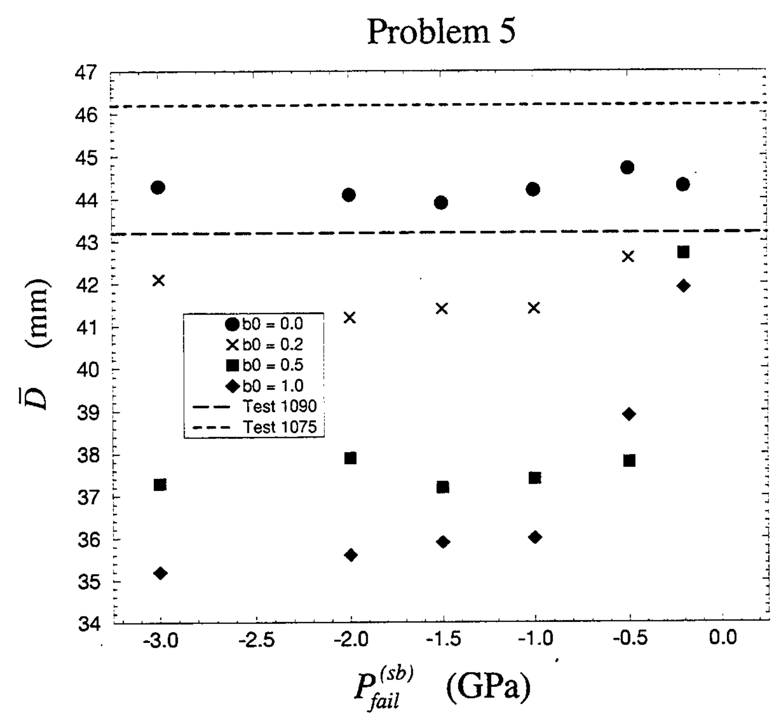

Figure 11: Final Through-Thickness-Averaged Hole Diameter vs. Spall Pressure of Shear-Banded RHA From Problem 5.

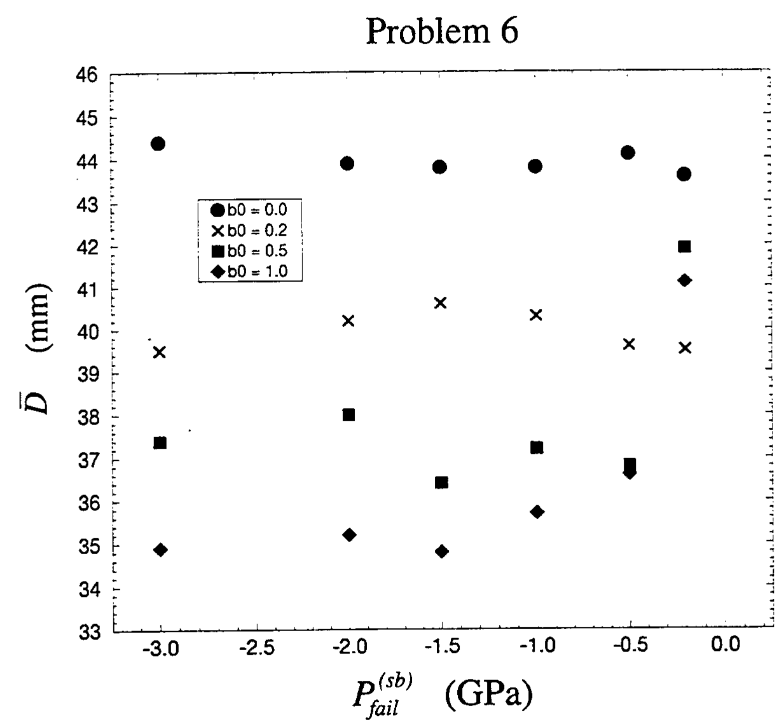

Figure 12: Final Through-Thickness-Averaged Hole Diameter vs. Spall Pressure of Shear-Banded RHA From Problem 6.

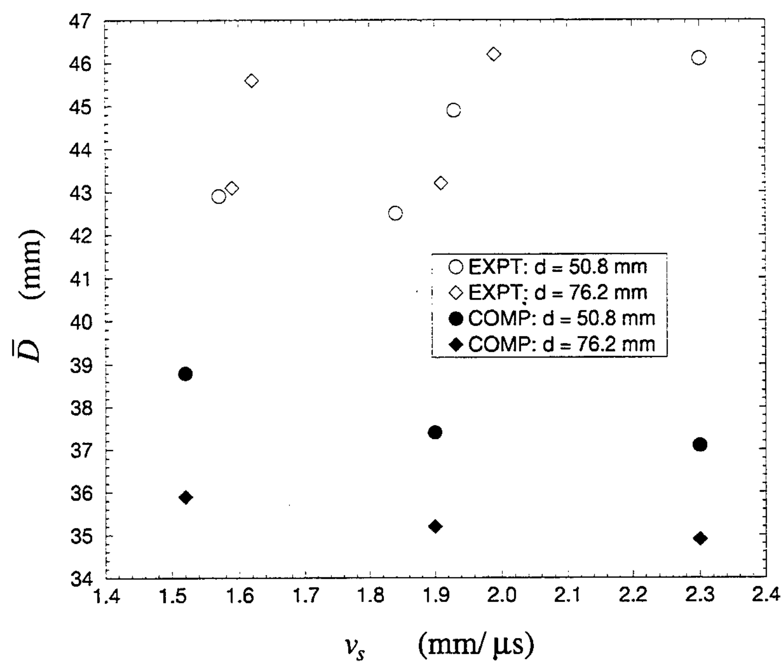

Figure 13: Final Through-Thickness-Averaged Hole Diameter vs. Striking Speed From Problems 1 Through 6 for $P_{fail}^{(sb)} = -3.0\,\mathrm{GPa}$ and $b_o = 1.0$.

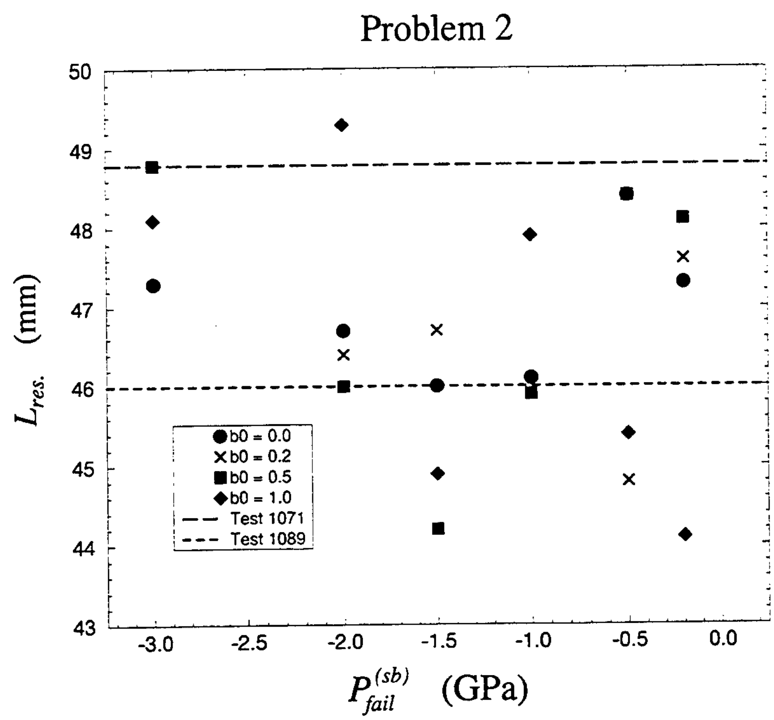

Figure 14: Residual Rod Length vs. Spall Pressure of Shear-Banded RHA From Problem 2.

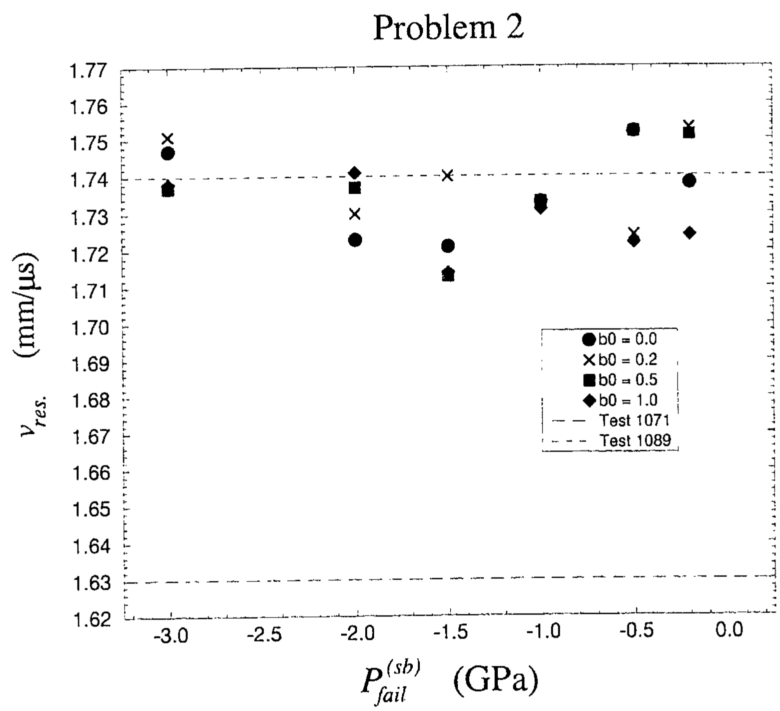

Figure 15: Residual Rod Speed vs. Spall Pressure of Shear-Banded RHA From Problem 2.

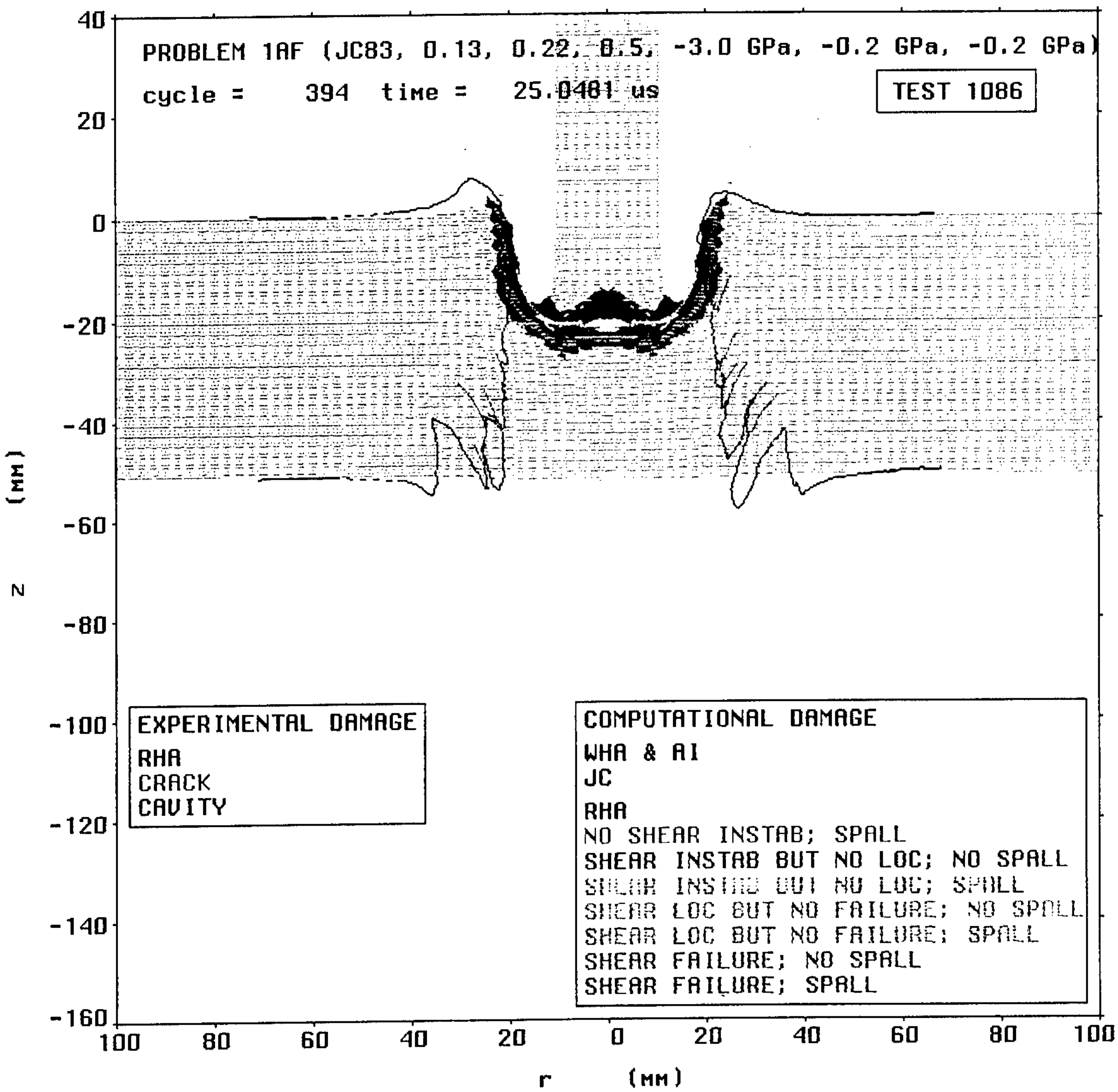

Figure 16: Mesh Plot at 25 μs After Impact From Problem 1 with $P_{fail}^{(sb)} = -3.0$ GPa and $b_o = 0.5$.

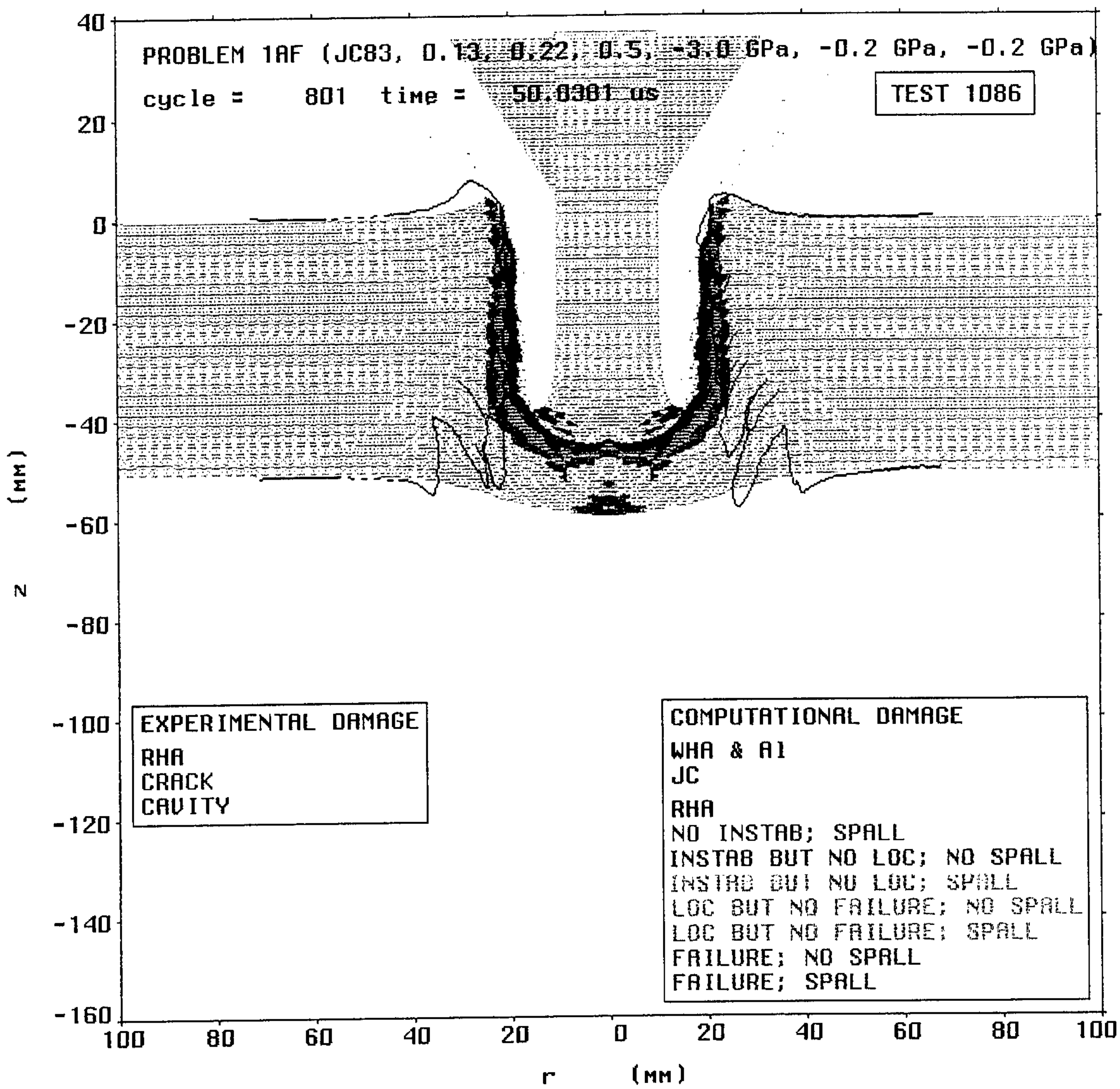

Figure 17: Mesh Plot at 50 μs After Impact From Problem 1 with $P_{fail}^{(sb)} = -3.0$ GPa and $b_o = 0.5$.

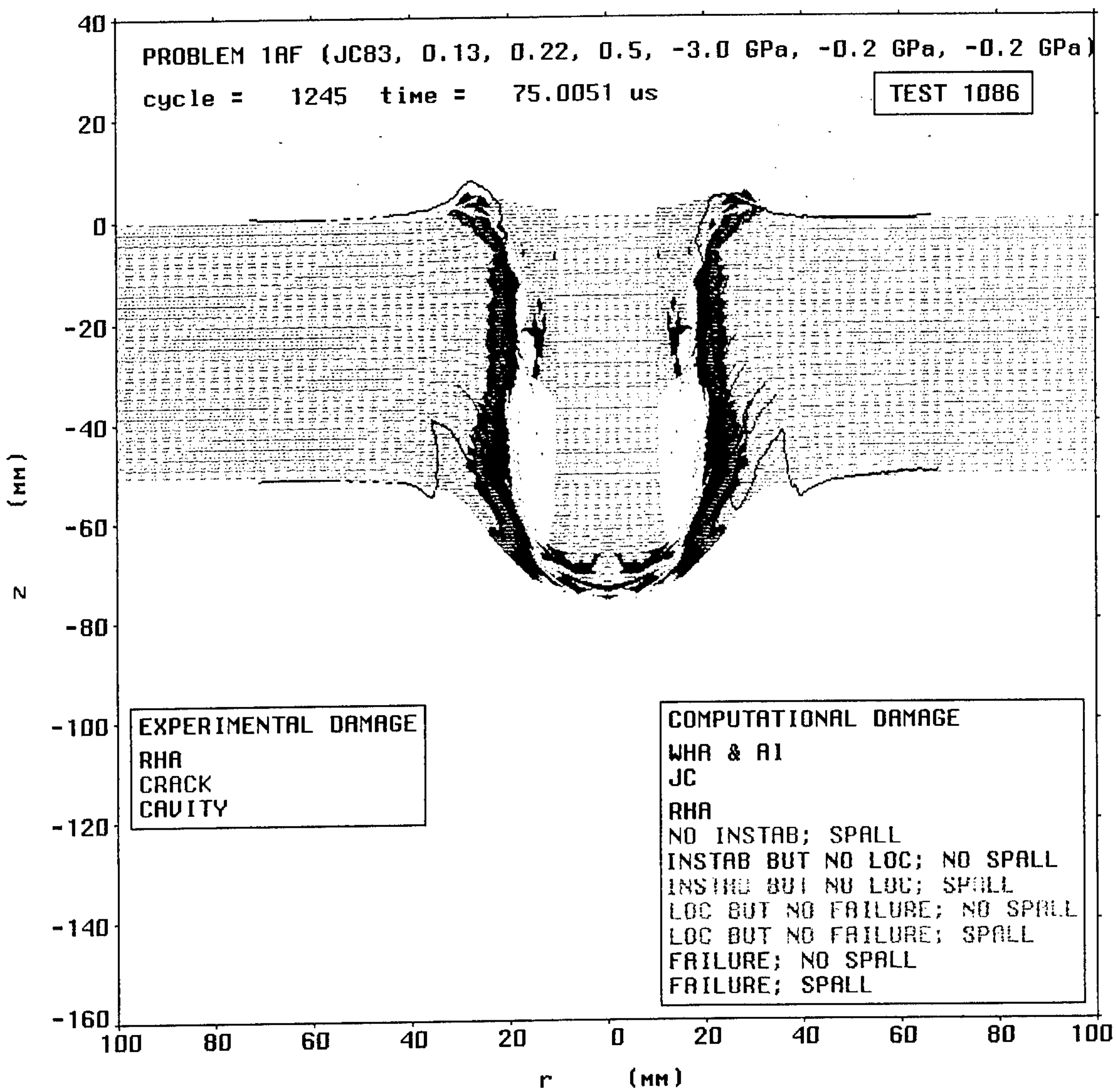

Figure 18: Mesh Plot at 75 μs After Impact From Problem 1 with $P_{fail}^{(sb)} = -3.0$ GPa and $b_o = 0.5$.

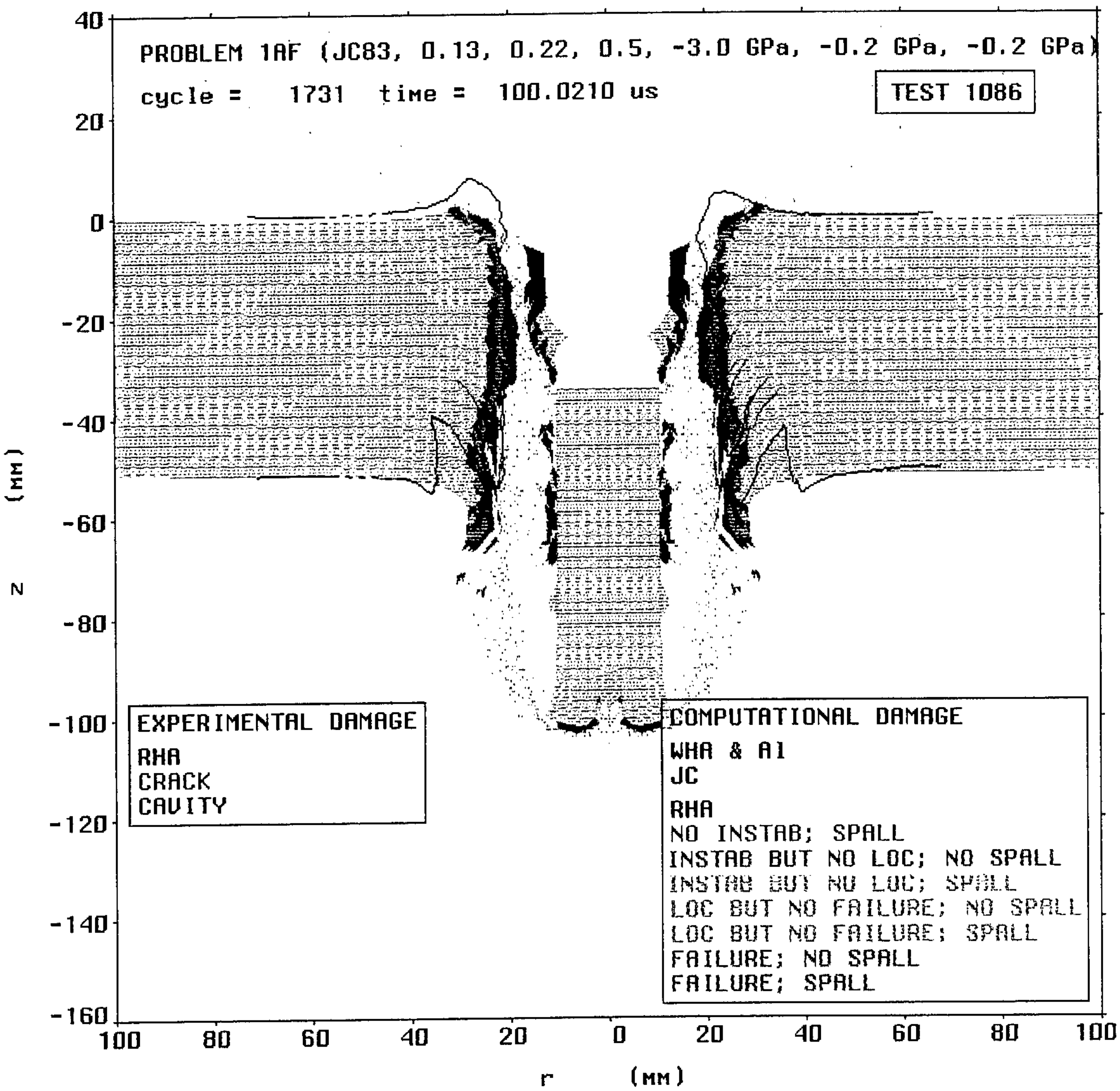

Figure 19: Mesh Plot at 100 μs After Impact From Problem 1 with $P_{fail}^{(sb)} = -3.0$ GPa and $b_o = 0.5$.

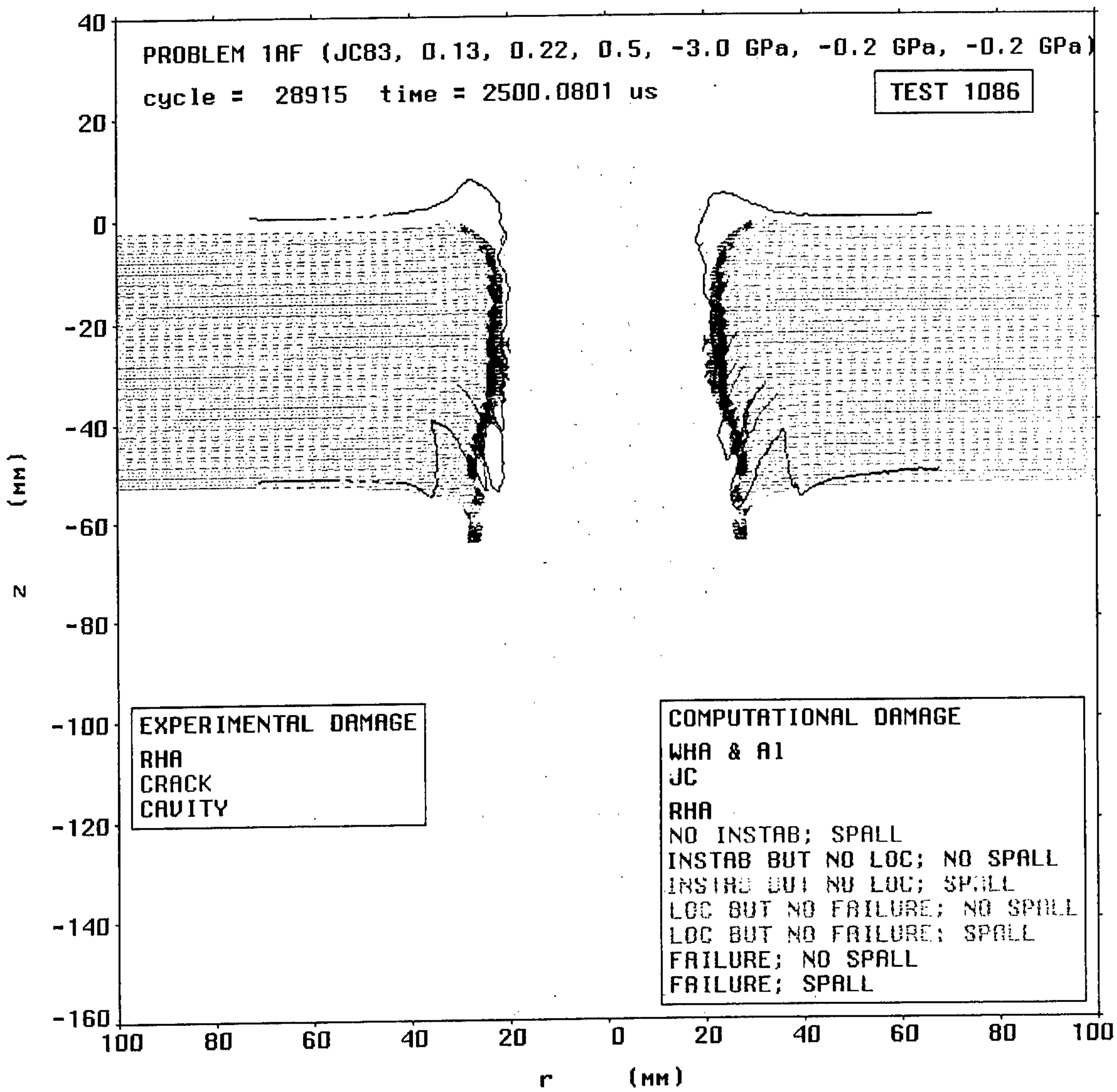

Figure 20: Mesh Plot at 2500 μs After Impact From Problem 1 with $P_{fail}^{(sb)} = -3.0$ GPa and $b_o = 0.5$.

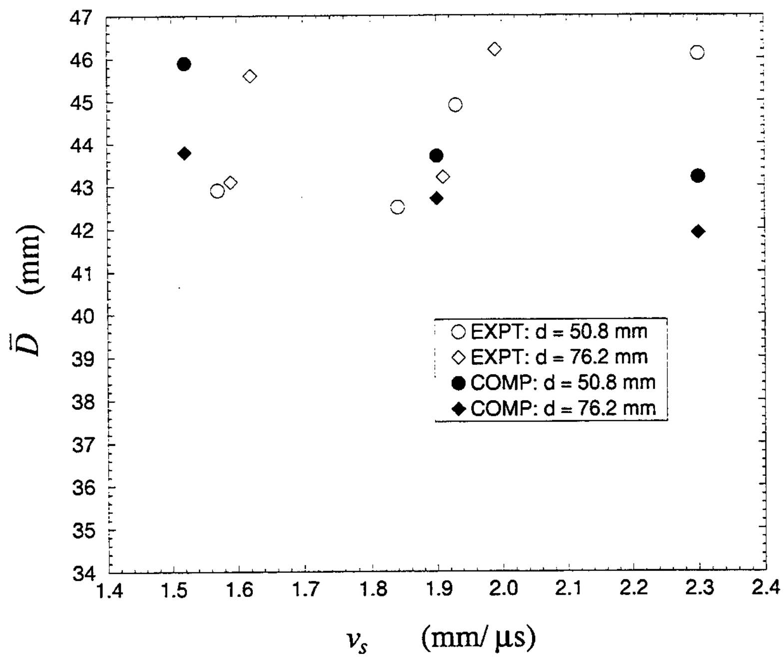

Figure 21: Final Through-Thickness-Averaged Hole Diameter vs. Striking Speed From Problems 1 Through 6 for $P_{fail}^{(sb)} = -0.2$ GPa and $b_o = 0.5$.

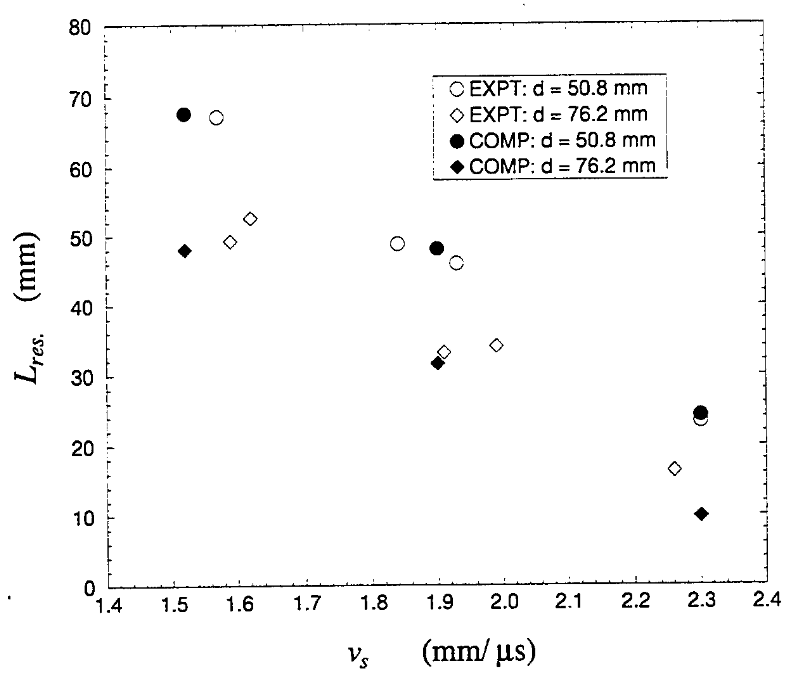

Figure 22: Residual Rod Length vs. Striking Speed From Problems 1 Through 6 for $P_{fail}^{(sb)} = -0.2$ GPa and $b_o = 0.5$.

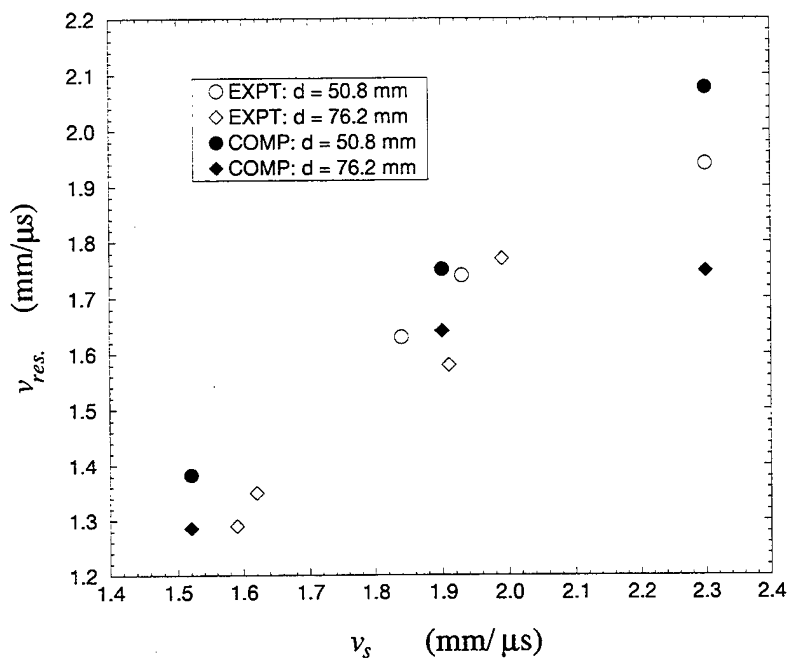

Figure 23: Residual Rod Speed vs. Striking Speed From Problems 1 Through 6 for $P_{fail}^{(sb)} = -0.2$ GPa and $b_o = 0.5$.

INTENTIONALLY LEFT BLANK.

5 References

Bai, Y. L. "Thermo-Plastic Instability in Simple Shear." *Journal for the Mechanics and Physics of Solids*, vol. 30, pp. 195–207, 1982.

Batra, R. C. "The Initiation and Growth of, and the Interaction Among, Adiabatic Shear Bands in Simple and Dipolar Materials." *International Journal of Plasticity*, vol. 3, pp. 75–89, 1987.

Bless, S. J. "Spall Criteria for Several Metals." AFWAL-TR-81-4040, Air Force Wright Aeronautical Laboratories, Wright-Patterson AFB, OH, 1981.

Camacho, G. T., and M. Ortiz. "Adaptive Lagrangian Modelling of Ballistic Penetration of Metallic Targets." *Computer Methods in Applied Mechanics and Engineering*, vol. 142, pp. 269–301, 1997.

Chichili, D. R. "High-Strain-Rate Deformation Mechanisms and Adiabatic Shear Localization in Alpha-Titanium." Doctoral Dissertation, The Johns Hopkins University, Baltimore, MD, 1997.

Chichili, D. R., and K. T. Ramesh. "Recovery Experiments for Adiabatic Shear Localization: A Novel Experimental Technique." *Journal of Applied Mechanics*, vol. 66, pp. 10–20, 1999.

Chichili, D. R., K. T. Ramesh, and K. J. Hemker. "The High-Strain-Rate Response of Alpha-Titanium: Experiments, Deformation Mechanisms and Modeling." *Acta materiala*, vol. 46, pp. 1025–1043, 1998.

Cho, K, Y. C. Chi, and J. Duffy. "Microscopic Observations of Adiabatic Shear Bands in Three Different Steels." *Metallurgical Transactions*, vol. 21A, pp. 1161–1175, 1990.

Hauver, G. E. "The Hugoniot for 90W–7Ni–3Fe Tungsten Alloy." BRL-MR-2987, U.S. Army Ballistic Research Laboratory, Aberdeen Proving Ground, MD, 1980.

Honeycombe, R. W. K. *Steels, Microstructure and Properties.* London: Edward Arnold, pp. 94–96, 1981.

Irwin, C. J. "Metallographic Interpretation of Impacted Ogive Penetrators." DREV R-652/72, Defence Research Establishment, Valcartier, Quebec, 1972.

Johnson, G. R. Private Communication. 1997.

Johnson, G. R., and W. H. Cook. "A Constitutive Model and Data for Metals Subjected to Large Strains, High Strain Rates and High Temperatures." *Proceedings of the Seventh International Ballistics Symposium*, The Hague, pp. 541–547, 1983.

Johnson, G. R., and W. H. Cook. "Fracture Characteristics of Three Metals Subjected to Various Strains, High Strain Rates, Temperatures and Pressures." *Engineering Fracture Mechanics*, vol. 21, pp. 31–48, 1985.

Johnson, G. R., and R. A. Stryk. "User Instructions for the 1992 Version of the EPIC Research Code." Alliant Techsystems, Inc., Brooklyn Park, MN, 1992.

Johnson, G. R., and R. A. Stryk. "An Automatic Sliding Interface Algorithm for Intense Impulsive Loading Computations." *Communications in Numerical Methods in Engineering*, vol. 12, pp. 885–896, 1996.

Kerley, G. I. "Multiphase Equation of State for Iron." SAND93-0027, Sandia National Laboratories, Kirtland Air Force Base, NM, 1993.

Kohn, B. J. "Compilation of Hugoniot Equations of State." AFWL-TR-69-38, Air Force Weapons Laboratory, Kirtland Air Force Base, NM, 1969.

Malvern, L. E. *Introduction to the Mechanics of a Continuous Medium.* New York: Prentice-Hall, pp. 336–373, 1969a.

Malvern, L. E. *Op. cit.*, p. 364, 1969b.

Marchand, A., and J. Duffy. "An Experimental Study of the Formation Process of Adiabatic Shear Bands in a Structural Steel." *Journal for the Mechanics and Physics of Solids*, vol. 36, pp. 251–283, 1988.

McGlaun, J. M., S. L. Thompson, L. N. Kmetyk, and M. G. Elrick. "A Brief Description of the Three-Dimensional Shock Wave Code CTH." SAND89-0607, Sandia National Laboratories, Kirtland Air Force Base, NM, 1990.

Molinari, A., and R. J. Clifton. "Analytical Characterization of Shear Localization in Thermoviscoplastic Materials." *Journal of Applied Mechanics*, vol. 54, pp. 806–812, 1987.

Raftenberg, M. N. "Lagrangian Hydrocode Simulations of Rolled-Homogeneous-Armor Plate Perforation by a Shaped Charge Jet." *International Journal of Impact Engineering*, vol. 15, pp. 619–643, 1994.

Raftenberg, M. N. "Steel Plate Perforation by Small L/D Tungsten Rods: Effects of Strength, Equation of State, and Drag Flare." *Structures Under Extreme Loading Conditions - 1996*, PVP–Vol. 325, edited by Y. S. Shin and J. A. Zukas, ASME, New York, pp. 205–220, 1996a.

Raftenberg, M. N. "Strength, Equation of State, and Drag Flare Effects on Steel Plate Perforation by Small Length-to-Diameter Ratio Tungsten Rods." ARL-TR-1052, U.S. Army Research Laboratory, Aberdeen Proving Ground, MD, p. 73, 1996b.

Raftenberg, M. N., and E. W. Kennedy. "Steel Plate Perforation by Tungsten Rods of Small L/D." *Proceedings of the Fifteenth International Ballistics Symposium*, vol. 1, Jerusalem, pp. 315–321, 1995.

Raftenberg, M. N., and C. D. Krause. "Metallographic Observations of Armor Steel Specimens from Plates Perforated by Shaped Charge Jets." *International Journal of Impact Engineering*, vol. 23, pp. 757–770, 1999.

Rajendran, A. M., M. A. Dietenberger, and D. J. Grove. "A Void Browth Based Failure Model to Describe Spallation." *Journal of Applied Physics*, vol. 65, pp. 1521–1527, 1989.

Ramesh, K. T. Private Communication. 1999.

Taylor, G. I., and H. Quinney. "The Latent Energy Remaining in a Metal After Coldworking." *Proceedings of the Royal Society (London)*, vol. A413, pp. 307–326, 1934.

U.S. Department of Defense. "Military Specification: Armor Plate, Steel, Wrought, Homogeneous (for Use in Combat Vehicles and for Ammunition Testing)." MIL-A-12560H, U.S. Army Materials Technology Laboratory, Watertown, MA, 1991.

Zhu, Z. G., and R. C. Batra. "Shear Band Development in a Thermally Softening Viscoplastic Body." *Computers & Structures*, vol. 39, pp. 459–472, 1991.

INTENTIONALLY LEFT BLANK.

List of Symbols

A, B, C	material constants in the Johnson-Cook strength model
D_1, D_2, D_3, D_4, D_5	material constants in the Johnson-Cook fracture model
$\overline{D}$	diameter of the final target perforation hole averaged over the thickness (associated with the computational solution at 2.5 ms after impact)
D_s	striking diameter of the WHA rod
F	function of ρ, $\dot{\varepsilon}$, and θ in the algebraic equation governing ε^p_{inst}
G	elastic shear modulus
K_1, K_2, K_3	material-constant coefficients in the shock-Hugoniot/compression relation
L_{res}	length of the WHA residual (associated with the computational solution at 2.5 ms after impact)
L^{comp}_{res}	computational result for L_{res}
L^{exp}_{res}	experimental result for L_{res}
$L^{\vert comp-exp\vert}_{res}$	maximum observed absolute value of the difference between an L^{comp}_{res} and a specific L^{exp}_{res}
L_s	striking length of the WHA rod
M, N	material constants in the Johnson-Cook strength model
P	pressure
P_{loc}	pressure at the time step when localization strain is reached
P_{fail}	spall pressure; a function of ε^p and P_{loc}
$P^{(sb)}_{fail}$	spall pressure in shear-banded material; a function of P_{loc}
$P^{(sb+)}_{fail}$	shear-banded spall pressure when localization initiated under hydrostatic compression; a material constant
$P^{(sb-)}_{fail}$	shear-banded spall pressure when localization initiated under hydrostatic tension; a material constant
$P^{(o)}_{fail}$	pre-shear-banded spall pressure; a material constant
P_H	shock-Hugoniot pressure; a function of μ
P_{shock}	shock pressure
Y	von Mises flow stress
Y_{JC}	von Mises flow stress according to the Johnson-Cook strength model

a_r, b_r, c_r	constant coefficients in the radial velocity shape function
a_z, b_z, c_z	constant coefficients in the axial velocity shape function
b	residual flow stress in a shear-banded element once the localization process is complete; a function of P_{loc}
b_o	the value of b for the case when localization initiated under hydrostatic compression; a material constant
c	specific heat
d	target plate thickness
r, z	radial, axial coordinates
t	time
v_r, v_z	radial, axial velocity
v_{res}	speed of the WHA residual (associated with the computational solution at 2.5 ms after impact)
v_{res}^{comp}	computational result for v_{res}
v_{res}^{exp}	experimental result for v_{res}
v_s	striking speed of the WHA rod
v_s^{comp}	computational striking speed of the WHA rod
v_s^{exp}	experimentally achieved striking speed of the WHA rod
v_{shock}	shock-wave speed
ΔL^{exp}	experimental result for the net rod shortening
Δv_{max}^{comp}	maximum computational value observed for the net rod deceleration
Δv_{min}^{comp}	minimum computational value observed for the net rod deceleration
Δv^{exp}	experimental result for the net deceleration of the WHA rod
$\Delta\varepsilon_{fail}^p$	difference between equivalent plastic strains at which localization begins and ends; a material constant
$\Delta\varepsilon_{loc}^p$	difference between equivalent plastic strains at which instability occurs and localization begins; a material constant
Γ	Grüneison coefficient
β	fraction of plastic work converted to heat (Taylor-Quinney constant)
ε^p	equivalent plastic strain
ε_{fail}^p	equivalent plastic strain at completion of localization ("failure strain")
ϵ_{ij}^p	Cartesian components of plastic strain
ε_{loc}^p	equivalent plastic strain at initiation of localization ("localization strain")

ε^p_{inst} equivalent plastic strain corresponding to maximum stress on the applicable constant-strain-rate adiabatic stress-plastic strain curve ("instability strain")

ε^f_{min} a material constant in the Johnson-Cook fracture model

$\dot{\varepsilon}^p$ time rate of change of equivalent plastic strain

μ compression

ρ density

ρ_o undeformed density

σ_{fail} spall axial-stress

σ_{spall} a material constant in the Johnson-Cook fracture model

σ'_{ij} Cartesian components of deviatoric Cauchy stress

θ temperature

θ_m melt temperature

θ_r room temperature

INTENTIONALLY LEFT BLANK.

NO. OF COPIES	ORGANIZATION
2	DEFENSE TECHNICAL INFORMATION CENTER DTIC DDA 8725 JOHN J KINGMAN RD STE 0944 FT BELVOIR VA 22060-6218
1	HQDA DAMO FDQ D SCHMIDT 400 ARMY PENTAGON WASHINGTON DC 20310-0460
1	OSD OUSD(A&T)/ODDDR&E(R) R J TREW THE PENTAGON WASHINGTON DC 20301-7100
1	DPTY CG FOR RDA US ARMY MATERIEL CMD AMCRDA 5001 EISENHOWER AVE ALEXANDRIA VA 22333-0001
1	INST FOR ADVNCD TCHNLGY THE UNIV OF TEXAS AT AUSTIN PO BOX 202797 AUSTIN TX 78720-2797
1	DARPA B KASPAR 3701 N FAIRFAX DR ARLINGTON VA 22203-1714
1	NAVAL SURFACE WARFARE CTR CODE B07 J PENNELLA 17320 DAHLGREN RD BLDG 1470 RM 1101 DAHLGREN VA 22448-5100
1	US MILITARY ACADEMY MATH SCI CTR OF EXCELLENCE DEPT OF MATHEMATICAL SCI MADN MATH THAYER HALL WEST POINT NY 10996-1786

NO. OF COPIES	ORGANIZATION
1	DIRECTOR US ARMY RESEARCH LAB AMSRL DD 2800 POWDER MILL RD ADELPHI MD 20783-1197
1	DIRECTOR US ARMY RESEARCH LAB AMSRL CS AS (RECORDS MGMT) 2800 POWDER MILL RD ADELPHI MD 20783-1145
3	DIRECTOR US ARMY RESEARCH LAB AMSRL CI LL 2800 POWDER MILL RD ADELPHI MD 20783-1145
	ABERDEEN PROVING GROUND
4	DIR USARL AMSRL CI LP (BLDG 305)

NO. OF COPIES	ORGANIZATION
4	DIR USARO D STEPP K IYER J WU TECH LIB PO BOX 12211 RSCH TRI PK NC 27709-2211
1	CDR USATACOM AMSTA RSK J THOMPSON WARREN MI 48397-5000
5	CDR USARDEC AMSTA AEE WW E BAKER C CHIN R FONG J PEARSON TECH LIB PICATINNY ARSENAL NJ 07806-5000
1	CDR USARDEC AMSTA AET M TECH LIB PICATINNY ARESENAL NJ 07806-5000
1	CDR USARDEC AMSTA FS E ANDRICOPOULOS PICATINNY ARESENAL NJ 07806-5000
3	CDR US ARMY MERDEC AMSMI RD ST WF L CRAFT D LOVELACE M SCHEXNAYDER REDSTONE ARSNL AL 35898
1	CDR USATACOM ARM APP SECT AMSTA RSK S GOODMAN WARREN MI 48397-5000
1	CDR US ARMY COE T BLEVINS 3909 HALL FERRY RD VICKSBURG MS 39180-6199

NO. OF COPIES	ORGANIZATION
3	DIR US ARMY DARPA J RICHARDSON B WILCOX TECH INFO 3701 N FAIRFAX DR ARLINGTON VA 22203-1714
1	DIR US ARO WASH AMXRO W K A BANNISTER RM 8N31 5001 EISENHOWER AVE ALEXANDRIA VA 22333-0001
4	CDR NAVAL SUR WAR CTR TECH LIB W H HOLT W MOCK D L DICKINSON DAHLGREN VA 22488
5	CDR NAVAL WPNS CTR CODE 3266 R HOFFMANN CODE 3261 T GILL S FINNEGAN J C SCHULZ TECH LIB CHINA LAKE CA 93555-6001
6	CDR NAVAL SUR WAR CTR C S COFFEY P PARK F ZERILLI CODE 4140 R K GARRET JR J MCKIRGAN TECH LIB 101 STRAUSS AVE INDIAN HEAD MD 20640
1	CDR NAVAL RSCH LAB J A NEMES WASH DC 20375
3	CDR NAVAL POSTGRAD SCH CODE 73J STERNBERG MONTEREY CA 93943
2	46 OG/OGML I S TALBOT J FLINT 104 CHEROKEE AVE EGLIN AFB FL 32542-5600

NO. OF COPIES	ORGANIZATION
1	USAF WRIGHT AERO LABS T NICHOLAS WRIGHT PAT AFB OH 45433
1	DIR PHILLIPS LAB F ALLAHDADI KIRTLAND AFB NM 87185
6	DIR WRIGHT LAB MNMW J A COLLINS W COOK J FOSTER JR D LAMBERT M NIXON TECH LIB EGLIN AFB FL 32542-5434
9	DIR SANDIA NAT LAB M KIPP L C CHHABILDAS R M BRANNON M FORRESTAL P A TAYLOR T TRUCANO P YARRINGTON E HERTEL S A SILLING PO BOX 5800 ALBUQUERQUE NM 87185-5800
3	DIR SANDIA NAT LAB D BAMMANN M CHIESA R A REGUERIO LIVERMORE CA 94551
2	UNIV OF DAYTON RES INST N BRAR A J PIEKUTOWSKI 300 COLLEGE PK DAYTON OH 45469
3	SRI INTRNAT D CURRAN L SEAMAN T SHOCKEY 333 RAVENSWOOD AVE MENLO PK CA 94025

NO. OF COPIES	ORGANIZATION
13	DIR LLNL L 38 M FINGER L 122 BOWMAN L 35 R COUCH R TIPTON D BAUM L GLENN M J MURPHY J REAUGH K WINER L 342 D LASSILA G GOUDREAU W H GOURDIN TECH LIB PO BOX 808 LIVERMORE CA 94550
18	DIR LANL J CHAPYAK MS F663 J JOHNSON MS F663 T F ADAMS MS F663 D A MANDEL MS B216 J W HOPSON MS B295 K HOLIAN MS B295 G T GRAY III F ADDESSIO J BOLSTAD S R CHEN L HULL L LIBERSKY P MAULDIN D L PAISLEY L SCHWALBE J WALTER A ZUREK TECH LIB PO BOX 166 LOS ALAMOS NM 87454
3	SOUTHWEST RSCH INST DEPT OF MECH SCI C ANDERSON S MULLIN J WALKER 8500 CULEBRA RD SAN ANTONIA TX 02912

NO. OF COPIES	ORGANIZATION
1	INTL RSRCH ASSOC INC D ORPHAL 4450 BLACK AVE STE E PLEASANTON CA 94566
2	GEN RES CORP A CHARTERS T MENNA 5383 HOLLISTER AVE SANTA BARBARA CA 93111
4	ALLIANT TECHSYS INC S BEISSEL G JOHNSON R STRYK C WITTMAN 600 SECOND ST NE HOPKINS MN 55343
1	KAMAN SCI CORP J WILBECK 7600 BLVD S SUITE 208 HUNTSVILLE AL 35802
4	DYNA EAST CORP P C CHOU R CICCARELLI W FLIS M GRUDZA 3620 HORIZON DR KING OF PRUSSIA PA 19406-2647
1	AEROJET ELECTIC SYS CO WARHEAD SYSTEMS J CARLEONE PO BOX 296 AZUSA CA 91702
5	IAT G BESSETTE S BLESS H FAIR D LITTLEFIELD S SATAPATHY 4030 2 W BRAKER LN AUSTIN TX 78759-5329

NO. OF COPIES	ORGANIZATION
1	ZERNOW TECH SVC INC L ZERNOW 425W BENITA SUITE 208 SAN DIMAS CA 91773
1	ORLANDO TECH INC D MATUSKA PO BOX 855 SHALIMAR FL 32579
1	APPLIED RES ASSOC INC J YATTEAU 5941 S MIDDLEFIELD RD LITTLETON CO 80123
2	APPLIED RES ASSOC INC D E GRADY F MAESTAS 4300 SAN MATEO BLVD NE SUITE A 220 ALBUQUERQUE NM 87110
1	NETWORK COMPUTING SERVICES INC T J HOLMQUIST 1200 WASHINGTON AVE SOUTH MINNEAPOLIS MN 55415
1	JOHNS HOPKINS UNIVERSITY DEPT MECH ENGINEERING K T RAMESH BALTIMORE MD 21218
1	LIVERMORE SOFTWARE TECHNOLOGY CORP J O HALLQUIST 2876 WAVERLEY WAY LIVERMORE CA 94550-1740
1	NORTH CAROLINA STATE UNIV DEPT MECH AND AEROSPACE ENGINEERING M A ZIKRY BOX 7910 RALEIGH, NC 27695-7910

NO. OF COPIES	ORGANIZATION
2	CALIFORNIA INST OF TECH AERONAUTICS AND APPLIED MECHANICS M ORTIZ G RAVICHANDRAN MAIL CODE 105 50 PASADENA CA 91125
4	UNIV CA SAN DIEGO DEPT APPLIED MECHANICS M A MEYERS S NEMAT NASSER V F NESTERENKO K VECCHIO LA JOLLA CA 92093-0416
1	UNIV TEXAS EL PASO DEPT METALLURGY AND MATERIALS SCIENCE L E MURR EL PASO TX 79968
1	UNIV OF ALABAMA DEPT ENGRG MECHANICS S E JONES PO BOX 870278 TUSCALOOSA AL 34587-0278
1	TEXAS TECH UNIVERSITY DEPT MECHANICAL ENGRG V I LEVITAS BOX 41021 LUBBOCK TX 79409-1021
2	GEORGIA INST OF TECH WOODRUFF SCHOOL MECHANICAL ENGINEERING D L MCDOWELL M ZHOU ATLANTA GA 30332-0405
2	PURDUE UNIVERSITY B GAILLY H ESPINOSA WEST LAFAYETTE IN 47907

NO. OF COPIES	ORGANIZATION
1	VIRGINIA POLYTECHNIC INSTITUTE DEPT ENGRG SCIENCE R BATRA BLACKSBURG VA 65401-0219
1	UNIVERSITY OF MARYLAND DEPT MECHANICAL ENGRG R W ARMSTRONG COLLEGE PARK MD 20742
2	BROWN UNIVERSITY ENGINEERING DIVISION R CLIFTON A NEEDLEMAN BOX D B&H 6S PROVIDENCE RI 02912
3	NORTHWESTERN UNIV DEPT MECH ENGRG W K LIU 2145 SHERIDAN RD EVANSTON IL 60208-3111
1	NORTHWESTERN UNIVERSITY DEPT CIVIL ENGRG T BELYTSCHKO 2145 SHERIDAN RD EVANSTON IL 60208
1	NORTHWESTERN UNIVERSITY DEPT APPLIED MATH W E OLMSTEAD 2145 SHERIDAN RD EVANSTON IL 60208
2	NORTHWESTERN UNIVERSITY G OLSON C BRINSON 2145 SHERIDAN RD EVANSTON IL 60208
1	WASHINGTON STATE UNIV MECH AND MATLS ENG H ZBIB PULLMAN WA 99164-2920

NO. OF COPIES	ORGANIZATION
1	CORNELL UNIVERSITY A ZEHNDER KIMBALL HALL ITHACA NY 14853
1	ARIZONA STATE UNIV DEPT MECH AND AEROSPACE ENGRG D KRAJCINOVIC TEMPE AZ 85286-6106
1	SUNY STONY BROOK DEPT MATH SCI DR GLIMM STONY BROOK NY 11791
1	UNIV OF MISSOURI ROLLA DEPT OF CIVIL ENGINEERING W P SCHONBERG ROLLA MO 65409

ABERDEEN PROVING GROUND

NO. OF COPIES	ORGANIZATION
1	DSI J KINEKE BLDG 309
1	DIR USAMSAA R THOMPSON
1	LLNL G RANDERS PEHRSON BLDG 309
57	DIR USARL AMSRL SL BC J T KLOPCIC AMSRL SL BV R SHNIDMAN R SAUCIER J R STROBEL AMSRL SL B J SMITH AMSRL WM T B BURNS AMSRL WM I MAY AMSRL WM TD R BITTING M BOTELER

NO. OF COPIES	ORGANIZATION
	AMSRL WM TD J DANDEKAR A DIETRICH N GNIAZDOWSKI F GREGORY D J GROVE T FARRAND K FRANK P W KINGMAN M RAFTENBERG A RAJENDRAN E RAPACKI M SCHEIDLER S SCHOENFELD S SEGLETES T VOGLER T WEERASOORIYA AMSRL WM TC T BJERKE R COATES F GRACE E KENNEDY K KIMSEY M LAMPSON L MAGNESS S SCHEFFLER S SCHRAML G SILSBY B SORENSON W WALTERS AMSRL WM TA S BILYK W BRUCHEY G FILBEY W GILLICH W GOOCH Y HUANG D KLEPONIS H MEYER M NORMANDIA AMSRL WM TB R FREY R LOTTERO AMSRL WM T T WRIGHT AMSRL WM MB M GAZONAS D HOPKINS C HOPPEL AMSRL WM BC S WILKERSON

NO. OF COPIES	ORGANIZATION
	ABERDEEN PROVING GROUND (CONT)
	AMSRL WM MA R ADLER J BEATTY J WELLS M STAKER

NO. OF COPIES	ORGANIZATION
1	ERNST MACH INSTITUT FRAUNX HOFER INSTITUT V HOHLER ECKERSTR 4 7800 FREIBURG GERMANY
1	RAFAEL BALLISTICS CENTER M MAYSELESS PO BOX 2250 HAIFA ISRAEL
1	NATIONAL ACADEMY OF SCIENCES INSTITUTE PROBLEMS OF STRENGTH G V STEPANOV TIMIRYAZEV STR 2 252914 KIEV 14 UKRAINE
2	UNIVERSITE DE METZ LABORATOIRE DE PHYSIQUE ET MECHANIQUE DES MATERIAUX J R KLEPACZKO A MOLINARI ILE DE SAULCY 57045 METZ CEDEX 01 FRANCE
1	RUSSIAN ACADEMY OF SCIENCES INSTITUTE MICHANICAL ENGINEERING Y I MESCHERYAKOV 199178 ST PETERSBURG V O BOLSHOY 61 RUSSIA
1	TNO PRINS MAURITS LAB R IJSSELSTEIN LANGE KLEIWEG 137 PO BOX 45 2280 AA RIJSWIJK THE NETHERLANDS

NO. OF COPIES	ORGANIZATION
1	GIAT INDUSTRIES DIVISION DES SYSTEMES D ARMES ET DE MUNITIONS H COUQUE 7 ROUTE DE GUERRY 18023 BOURGES CEDEX FRANCE
2	DERA TERMINAL EFFECTS WX 5 I CULLIS J CURTIS FORT HALSTEAD SEVENOAKS KENT TNI4 7BP UNITED KINGDOM
1	TDW MANFRED HELD 86523 SCHROBENHAUSEN GERMANY

REPORT DOCUMENTATION PAGE

Form Approved OMB No. 0704-0188

1. AGENCY USE ONLY *(Leave blank)*	2. REPORT DATE	3. REPORT TYPE AND DATES COVERED
	April 2000	Final, Oct 98 - Jan 00

4. TITLE AND SUBTITLE
A Shear Banding Model for Penetration Calculations

5. FUNDING NUMBERS
1L162618AH80

6. AUTHOR(S)
Martin N. Raftenberg

7. PERFORMING ORGANIZATION NAME(S) AND ADDRESS(ES)
U.S. Army Research Laboratory
ATTN: AMSRL-WM-TD
Aberdeen Proving Ground, MD 21005-5069

8. PERFORMING ORGANIZATION REPORT NUMBER
ARL-TR-2221

9. SPONSORING/MONITORING AGENCY NAMES(S) AND ADDRESS(ES)

10. SPONSORING/MONITORING AGENCY REPORT NUMBER

11. SUPPLEMENTARY NOTES

12a. DISTRIBUTION/AVAILABILITY STATEMENT
Approved for public release; distribution is unlimited.

12b. DISTRIBUTION CODE

13. ABSTRACT *(Maximum 200 words)*

A model for introducing the effects of adiabatic shear banding into a penetration calculation was installed into the EPIC wavecode. These effects are deemed to be reduction in the ratio of flow stress to the value predicted by the Johnson-Cook strength model and increase in spall pressure. A strain-rate- and temperature-dependent instability strain is determined from small-amplitude perturbation of constant-strain-rate simple shear. Imposed alterations in flow stress ratio and spall pressure commence at the "localization strain," separated from the instability strain by a fixed strain increment. The alterations proceed linearly with increasing effective plastic strain and terminate after an additional fixed strain increment, at the "failure strain." The values imposed on the flow stress ratio and the spall pressure at the failure strain are functions of local pressure at the time step when localization strain was reached. The nonzero value imposed on the flow stress ratio in the case of positive localization pressure reflects the phenomenon of fracture suppression within a fully formed shear band. The two fixed strain increments are evaluated from a torsional Kolsky bar test. The pre-shear-banded spall pressure is evaluated from plate-on-plate impact data. The flow stress ratio and spall pressure at and beyond the failure strain introduce two currently "free" parameters. The model was applied to a set of problems involving steel plate perforation by a tungsten rod, and reasonable agreement with experiment was obtainable in terms of the final target hole size and the length and speed of the tungsten residual.

14. SUBJECT TERMS
computational penetration mechanics, adiabatic shear band, rolled homogeneous armor, damage modeling, spallation, perforation

15. NUMBER OF PAGES
59

16. PRICE CODE

17. SECURITY CLASSIFICATION OF REPORT	18. SECURITY CLASSIFICATION OF THIS PAGE	19. SECURITY CLASSIFICATION OF ABSTRACT	20. LIMITATION OF ABSTRACT
UNCLASSIFIED	UNCLASSIFIED	UNCLASSIFIED	UL

INTENTIONALLY LEFT BLANK.

USER EVALUATION SHEET/CHANGE OF ADDRESS

This Laboratory undertakes a continuing effort to improve the quality of the reports it publishes. Your comments/answers to the items/questions below will aid us in our efforts.

1. ARL Report Number/Author ARL-TR-2221 (Raftenberg) ______ Date of Report April 2000 ______

2. Date Report Received ______

3. Does this report satisfy a need? (Comment on purpose, related project, or other area of interest for which the report will be used.) ______

4. Specifically, how is the report being used? (Information source, design data, procedure, source of ideas, etc.) ______

5. Has the information in this report led to any quantitative savings as far as man-hours or dollars saved, operating costs avoided, or efficiencies achieved, etc? If so, please elaborate. ______

6. General Comments. What do you think should be changed to improve future reports? (Indicate changes to organization, technical content, format, etc.) ______

CURRENT ADDRESS

Organization

Name E-mail Name

Street or P.O. Box No.

City, State, Zip Code

7. If indicating a Change of Address or Address Correction, please provide the Current or Correct address above and the Old or Incorrect address below.

OLD ADDRESS

Organization

Name

Street or P.O. Box No.

City, State, Zip Code

(Remove this sheet, fold as indicated, tape closed, and mail.)

(DO NOT STAPLE)